Geomechanical Characterization of Marcellus Shale

Citation: Villamor Lora, Rafael, Ehsan Ghazanfari, and Enrique Asanza Izquierdo. "Geomechanical Characterization of Marcellus Shale." Rock Mechanics and Rock Engineering 49.9 (2016): 3403–3424.

As Published: http://dx.doi.org/10.1007/s00603-016-0955-7

Publisher: Springer Vienna

Persistent URL: http://hdl.handle.net/1721.1/105181

Version: Author's final manuscript: final author's manuscript post peer review, without publisher's formatting or copy editing

Rock Mech Rock Eng
DOI 10.1007/s00603-016-0955-7

ORIGINAL PAPER

Geomechanical Characterization of Marcellus Shale

Rafael Villamor Lora[1,3] · **Ehsan Ghazanfari**[1] · **Enrique Asanza Izquierdo**[2]

Received: 4 September 2015 / Accepted: 14 March 2016

Abstract Understanding the reservoir conditions and material properties that govern the geomechanical behavior of shale formations under in situ conditions is of vital importance for many geomechanical applications. The development of new numerical codes and advanced multi-physical (thermo-hydro-chemo-mechanical) constitutive models has led to an increasing demand for fundamental material property data. Previous studies have shown that deformational rock properties are not single-value, well-defined, linear parameters. This paper reports on an experimental program that explores geomechanical properties of Marcellus Shale through a series of isotropic compression (i.e. $\sigma_1 = \sigma_2 = \sigma_3$) and triaxial (i.e. $\sigma_1 > \sigma_2 = \sigma_3$) experiments. Deformational and failure response of these rocks, as well as anisotropy evolution, were studied under different stress and temperature conditions using single- and multi-stage triaxial tests. Laboratory results revealed significant nonlinear and pressure-dependent mechanical response as a consequence of the rock fabric and the occurrence of microcracks in these shales. Moreover, multi-stage triaxial tests proved to be useful tools for obtaining failure envelopes using a single specimen. Furthermore, the anisotropic nature of Marcellus Shale was successfully characterized using a three-parameter coupled model.

Keywords Shale gas · Geomechanics · Laboratory characterization · Elasticity · Strength · Temperature · Anisotropy

List of symbols

σ_1	Major principal stress (axial stress)
σ_3	Minor principal stress (confining pressure)
p	Mean effective stress (i.e. $p = (\sigma_1 + 2\sigma_3)/3$)
q	Differential stress (i.e. $q = \sigma_1 - \sigma_3$)
ε_a	Axial strain
ε_r	Radial strain
ε_v	Volumetric strain (i.e. $\varepsilon_v = \varepsilon_a + 2\varepsilon_r$)
ε_s	Distortional strain (i.e. $\varepsilon_s = 2/3(\varepsilon_a - \varepsilon_r)$
σ_d	Dilation threshold
σ_f	Peak (failure) strength
σ_u	Ultimate strength
β	Orientation of the failure plane with respect the maximum principal stress
IC	Isotropic Compression stage (i.e. $\sigma_1 = \sigma_2 = \sigma_3$)
MSE	Elastic Multi Stage triaxial test
MSF	Failure Multi Stage triaxial test
SS	Single Stage triaxial test
SST	Single Stage triaxial test at high Temperature
ThC	Thermal Consolidation stage
TX	Triaxial stage (i.e. $\sigma_1 > \sigma_2 = \sigma_3$)
VTI	Vertical Transverse Isotropy

✉ Rafael Villamor Lora
villamor@mit.edu

[1] Department of Civil and Environmental Engineering, University of Vermont, Burlington, VT, USA

[2] Laboratorio de Geotecnia, Centro de Estudios y Experimentación, CEDEX, Madrid, Spain

[3] Present Address: Department of Civil and Environmental Engineering, Massachusetts Institute of Technology, Cambridge, MA, USA

Published online: 06 April 2016

1 Introduction

Geomechanical behavior of shales has drawn significant attention in recent years due to their role in a number of petroleum and civil engineering related issues (Ferrari and Laloui 2013). They include borehole stability modeling, lithology identification, exploitation of shale-oil and shale-gas reservoirs, and geological storage of CO_2, to name a few (Islam and Skalle 2013). This growing interest is largely driven by their notable contribution to the world's gas reserves (EIA 2013). Shale rocks, sometimes referred to as mudstones, are composed of extremely fine particles (typically less than 4 μm), resulting in rocks with permeabilities in the nano-Darcy range (Britt and Schoeffler 2009; Vermylen 2011; Ghassemi and Suarez-Rivera 2012). Though many shales look similar to the naked eye, their mineralogy and total organic content (TOC) exhibit a wide range in composition (Passey et al. 2010; Sone and Zoback 2013a).

1.1 Background

Achieving economic production in shale formations requires hydraulic fracturing stimulation of the reservoir to create an extensive and dense fracture network for the hydrocarbons to flow to the wellbore (Maxwell 2011). Major problems here are related to the variability and unpredictability of the outcome of these operations, along with sustaining the permeability in the long-term (Ghassemi and Suarez-Rivera 2012). It is therefore is of vital importance to understand the in situ conditions and material properties that govern fracture initiation, -propagation and -closure under reservoir conditions of pressure, pore fluid saturation, and temperature.

Industry standards commonly focus on the evaluation of a single set of parameters, such as the brittleness of the shale formation (Rickman et al. 2008), during the identification of prospective intervals for stimulation (Safari et al. 2014). While these approaches might successfully predict hydraulic fracturing potential, they are insufficient to describe the complex geomechanical behavior of shale formations (Sone 2012). Note that only about 15 % of the gas content of the shale stratum can be extracted with current industry practices (Bažant et al. 2014), and almost half of the wells still underperform (Maxwell 2011).

To date, hydraulic fracturing mechanisms are poorly understood, and numerical models cannot yet precisely predict fracture growth. In fact, as pointed by Davies et al. (2012), our knowledge about the propagation of fractures under in situ conditions comes mainly from industry experience (e.g. King et al. 2008; Fisher and Warpinski 2012) and field examples of natural hydraulic fractures (e.g. Lacazette and Engelder 1992; Savalli and Engelder 2005; Engelder et al. 2009).

It is commonly accepted that hydraulic fractures initiate when fluid pressure surpasses the minimum principal stress and the tensile strength of the shale. Then, fractures propagate in the direction perpendicular to the minimum principal stress. Alongside this tensile fracturing, shear of pre-existing fractures may occur in the vicinity of the stimulated volume in response to changes in stress magnitude and -orientation, that are associated with the injection of large volumes of water (Maxwell 2011). Moreover, shear deformation has also been observed in crack propagation and coalescence in shale (Morgan and Einstein 2014). Therefore, advanced analytical and computational models should integrate multiple modes of failure to represent the actual geomechanical behavior of shale reservoirs. Not surprisingly, simulation of shale behavior undergoing thermo-hydro-chemo-mechanical (THCM) processes is quite an active area in modern geomechanics (for a review see e.g. Buscarnera et al. 2014). This growing interest in the development of new models has led to an increasing demand for governing laws, and other fundamental material property data (Bažant et al. 2014; Safari et al. 2014).

Furthermore, understanding deformational properties becomes a fundamental task to better optimize operational procedures in shale gas reservoirs (Jacobi et al. 2008; Britt and Schoeffler 2009; Sone 2012; Ghassemi and Suarez-Rivera 2012). Shales are the most ubiquitous sedimentary rock, and they have been characterized in the past. Nevertheless, the development of unconventional (low-permeability) shale gas reservoirs has required adapting the traditional laboratory characterization techniques to the complex properties of these rocks. Workflows for systematic shale characterization in the laboratory (Dewhurst and Siggins 2006; Britt and Schoeffler 2009; Dewhurst et al. 2011; Josh et al. 2012) usually include a series non-destructive and destructive petrophysical and geomechanical testing methods. Potential challenges in geomechanical characterization are related to:

- *Strength and deformational behavior*. Important geomechanical parameters for these rocks include Young's modulus, Poisson's ratio, friction coefficient, cohesion, and unconfined compressive strength. The estimation of such parameters is typically addressed through a series of triaxial compression tests. These tests can be conducted either in dry, drained or undrained conditions, and may consist on multiple confining stages. Multi-stage triaxial compression experiments are often used as validated alternatives for the construction of failure envelopes with only one rock specimen, but also as good methods to eliminate

specimen variability (e.g. Yang 2012). Of special interest are also the relationships between geomechanical parameters with the rock fabric, petrophysical and dynamic properties (e.g. Sone and Zoback 2013a).

- *Anisotropy*. This is usually determined through a series of triaxial compression tests on rock specimens cored in different directions. Also, an efficient way to study both intrinsic and stress-induced anisotropy is through the single core plug approach utilizing the sonic pulse method (Dewhurst and Siggins 2006; Sarout and Guéguen 2008a; Dewhurst et al. 2011; Kuila et al. 2011). This experimental methodology allows one to fully characterize elastic anisotropy through elastic wave velocity measurements on a single specimen subjected to triaxial loading conditions.
- *Thermo-hydro-chemo-mechanical coupling*. Geomechanical characterization of shales is somewhat incomplete if reservoir conditions are not considered. Also, operational procedures in these reservoirs induce THCM environmental changes that may play an important role in shale mechanical response (Horsrud 2001; Eseme et al. 2007; Ghassemi and Suarez-Rivera 2012; Islam and Skalle 2013; Mohamadi et al. 2013; Hu and Hueckel 2013; Bauer et al. 2014).
- *Viscoelasticity-plasticity* (*creep*). The investigation of the time-dependent behavior of shale is also essential due to this behavior's role, among other effects, in the long-term transport properties (forecast hydrocarbon production models) and in situ stress evolution, with important implications for hydraulic fracturing (e.g. Ghassemi and Suarez-Rivera 2012; Sone and Zoback 2013b).

Notwithstanding the fact that the shale energy revolution has prompted increased research on shale rock characterization, there is still a lack of laboratory data for the largest shale reservoir in the United States, the Marcellus Shale. Engelder (2009) estimated that these black, organic-rich shales hold about 489 trillion cubic feet of gas (Kargbo et al. 2010). Therefore, many researchers are currently focusing on this play, and accordingly, the demand of fundamental rock property data is constantly increasing.

1.2 Objective and Main Goals

This study reports on an experimental program to explore geomechanical properties of Marcellus Shale. The main goal was to generate a geomechanical data set that can be used for numerical simulation. A total of nine isotropic compression (i.e. $\sigma_1 = \sigma_2 = \sigma_3$) and monotonic triaxial (i.e. $\sigma_1 > \sigma_2 = \sigma_3$) tests were performed in order to evaluate the deformability, and failure response of Marcellus Shale specimens as a function of confining pressure and temperature. Moreover, two multi-stage triaxial tests were conducted to further investigate the recoverable (elastic) and permanent (plastic) deformation of these nonlinear materials, and the suitability of such tests to obtain a full suite of geomechanical parameters from a single specimen. Additional characterization includes mineralogy, porosity, and fabric through thin section -and computer tomography analysis. Viscoelastic-plastic behavior is not addressed in the present paper, but additional laboratory data on the time-dependent response as a function of confining pressure and temperature can be found in Villamor Lora (2015).

The methodology presented in this study allowed us to conduct a specimen variability analysis, and resulted in relatively consistent laboratory results. This approach facilitated the development of a number of empirical relationships for the tested shale. Failure was further analyzed through the widely used Coulomb criteria (Jaeger et al. 2007) and Hoek–Brown model (Hoek and Brown 1980). Anisotropic behavior was also studied combining laboratory results from isotropic compression and triaxial tests. Exhaustive mechanical anisotropy characterization usually requires sophisticated equipment, or multiple specimens cored in different directions (with the consequent data scatter due to specimen variability). To overcome this limitation, this study made use of the so-called Vertical Transversely Isotropic coupling model (Puzrin 2012) that reduces the original independent parameters of the elastic tensor from five to three.

2 Materials

Shale specimens used in this study came from a whole core taken in a shallow well ($\sim$100 m deep) located at State Game Lands 252, Lycoming and Union counties, Allenwood, Pennsylvania (Fig. 1). The rock plugs were retrieved in 2009 by the Department of Geosciences at Pennsylvania State University, and stored at room temperature and ambient humidity conditions. All cores were oriented perpendicular to the bedding (vertical samples), hindering the characterization of anisotropy (see Sect. 3.3.1). Residual fluid content in these shales was found to be below 2 %, and it is considered low enough so that poroelastic effects can assumed to be negligible. Neither rehydration nor oven-drying were attempted in order to preserve mechanical properties. Although resaturation of shales is possible under controlled humidity conditions (Schmitt et al. 1994), such processes may change the internal structure and properties of the shale even when the manufactured pore fluid is assumed to match the original pore water chemical composition (Fjær et al. 2008). On the other hand, oven-drying may have lead to the loss of the clay-bound water

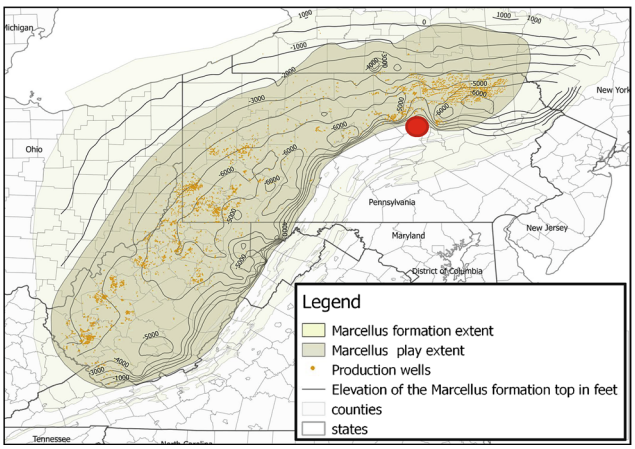

Fig. 1 Location map of drilled core that shows Marcellus formation (*light green*) and play (*dark green*) extents. Adapted from Thickness map of the Marcellus Formation, in EIA, retrieved March 7, 2016, from https://www.eia.gov/maps/pdf/marcellus-upd.pdf (color figure online)

possibly leading to drastic changes in mechanical properties.

2.1 Specimen Characterization

Mineralogy and petrological properties were studied via X-ray diffraction (XRD), whereas Total Organic Carbon (TOC) was measured by sample combustion. TOC is a fundamental parameter in assessing shale reservoirs potential, since it relates the total porosity to the gas content in the rock (Passey et al. 2010). Porosity was determined from the comparison of the bulk density of the rock with the average grain density (Mavko et al. 2009) measured in the XRD and TOC tests. The average material composition is summarized in Table 1.

For this study, shale specimens were selected from a depth between 95 and 115 m. Bulk density is fairly consistent within the interval with an average value of 2.58 ± 0.05 g/cm^3. These Marcellus Shale specimens have moderate organic content, with a TOC percentage of roughly 2.7 %. Porosity was determined to be close to 5 %, which is in good agreement with the trends found by Sone and Zoback (2013a), given the clay/kerogen content of the tested specimens. Previous studies have suggested that porosity in organic rich shales resides within the kerogen and/or clay minerals platelets (Passey et al. 2010; Sone and Zoback 2013a).

The XRD test revealed that clay and quartz minerals are the major constituents of the tested specimens (Table 1). Clay minerals in these shales were mostly from the mica group. Based on these laboratory results, this shale is composed of about 57.7 % clays (Mu/Ill + Ka + Chl), 35.9 % tectosilicates (Qrtz + Alb + Pyr), and 3.7 % carbonates (Dol + Ca).

It is well known that the mechanical behavior of shales is largely controlled by their microstructure (Josh et al. 2012). Due to their large heterogeneity at different scales, microstructure characterization of shales requires different multi-scale visualization techniques (Fig. 2). Rock fabric was studied via both scanning electron microscope (secondary and backscattered analysis) and optical microscopes with polarized light. In addition, post-mortem analysis of the cores was carried out using X-ray tomography for inspection of resulting fracture patterns.

Optical microscope images (Fig. 2e, f) exhibit macroscopic primary foliation (bedding) at different scales in the vertical (vh) plane. On the other hand, SEM images (Fig. 2g, h) reveal a microstructure consisting of a clayey matrix with silt grains and other various-shaped inclusions. Note that the preferential (sub-parallel to bedding) orientation in these shales is preserved across scales. Figure 2g shows a series of microcracks oriented subparallel to bedding. These horizontal fractures tend to increase the compliance in the direction perpendicular to the bedding, being also responsible for the initial nonlinear mechanical behavior. Moreover, porosity is not visible at this scale. Previous studies have shown that maximum pore throat in shales is in the micro and nanometer scale (Passey et al. 2010; Josh et al. 2012).

3 Experimental Techniques and Testing Plan

3.1 High Pressure Triaxial Apparatus

A series of triaxial compression experiments was conducted using a fully servo-controlled triaxial apparatus (AutoLab 1500). The experimental program used cylindrical specimens of rock plugs of 50.8 mm (2.0-in.) diameter with horizontal bedding planes (i.e. cylinder axis perpendicular to material deposition planes). Length/diameter aspect ratio was kept as close to 2 as possible.

Table 1 Material composition

Bulk density (g/cm^3)	Mineralogy (wt.%)								TOC (wt.%)	Porosity (%)
	Mu/Ill	Chl	Ka	Qrtz	Alb	Pyr	Dol	Ca		
2.58	38.3	15.7	3.6	29.1	4.2	2.6	2.7	1.1	2.7	5.0

Mu/Ill muscovite and illite, *Chl* chlorite, *Ka* kaolinite, *Qrtz* quartz, *Alb* albite, *Pyr* pyrite, *Dol* dolomite, *Ca* calcite

Deformation was measured by axial and radial self-temperature-compensated strain gauges installed on a copper sleeve. This copper sleeve also acts as a barrier between the specimen and the confining fluid. As shown in Fig. 3b, a maximum of four strain gauges were used simultaneously, usually two pairs consisting of one axial plus one radial gauge. These pairs of gauges were placed 90° with respect to each other, allowing one to check for potential anisotropic nature in the horizontal plane. In addition, a linear variable differential transformer (LVDT) measured the piston displacement, which was used to estimate axial strain when no strain gauge data were available.

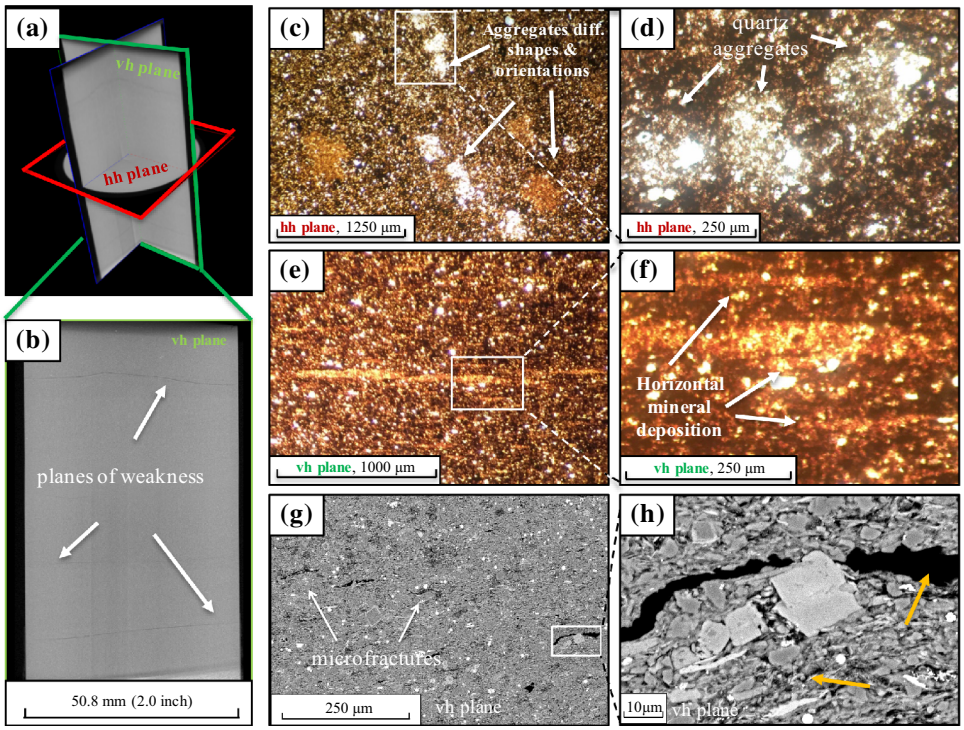

Fig. 2 Multi-scale visualization of Marcellus Shale. **a**, **b** CT-scan images of an intact core. At this scale, planes of weakness parallel to the bedding are visible. **c**–**f** Optical microscopic images taken from horizontal (**c**, **d**) and vertical (**e**, **f**) thin sections. On the one hand, the microstructure of the horizontal plane is characterized by the presence of aggregates with different shapes and orientations. On the other hand, primary foliation (bedding) is the main feature in the vertical plane. **g**, **h** Backscattered electron microscope images. Contrast in grey level in backscattered analysis reflects different material density. These images reveal a series of micro-cracks sub-parallel to the bedding, and the presence of voids with preferential (bed-parallel) orientations. Also, the clayey matrix with silt grains and other various-shaped inclusions is visible at this scale (*bottom yellow arrow* in **h**)

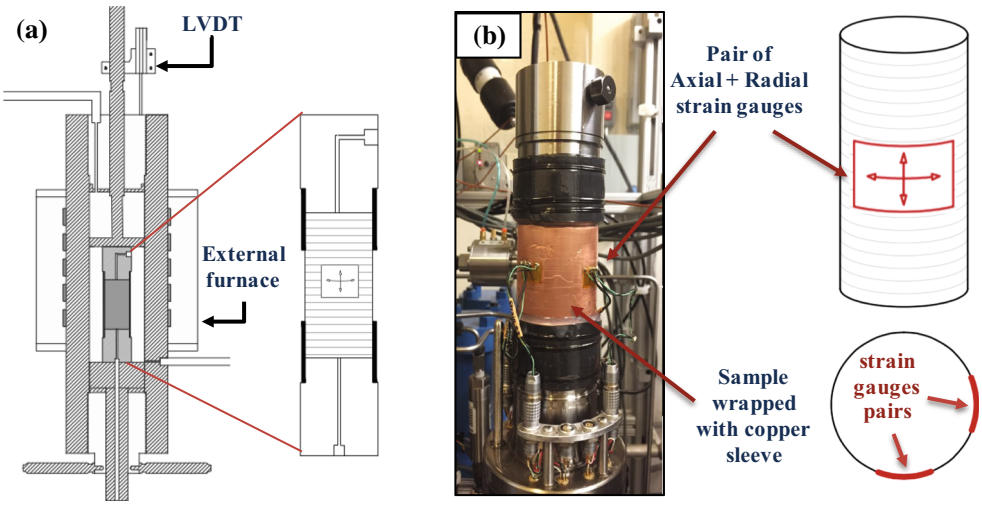

Fig. 3 **a** Layout of the triaxial apparatus used in the experiments. **b** Two pairs (axial + radial) of strain gauges installed on the copper sleeve

Heating of the specimens up to 120 °C is also possible using an external furnace embedded in the equipment. The temperature was measured using a thermal couple inside the cell in contact with the confining fluid.

Although the triaxial system includes pore pressure control, our tests were run under dry conditions for two main reasons. Firstly, available shale specimens were already room-dried, and the re-saturation process could damage the rock. Secondly, due to the low permeability of shales, a single drained test could take several weeks, even months (Dewhurst and Siggins 2006; Islam and Skalle 2013).

3.2 Testing Plan

Assessment of geomechanical parameters of gas shales is of fundamental importance in order to evaluate whether they will be suitable for hydraulic fracturing and keep the resulting fracture network open (Britt and Schoeffler 2009; Josh et al. 2012). In this paper the geomechanical behavior of Marcellus Shale was studied through a series of nine single stage (SS) and two multi stage (MS) triaxial compression tests.

3.2.1 Single Stage Triaxial Tests

The objective of this first set of tests was to study the geomechanical behavior of Marcellus Shale rocks under constant axial strain rate loading. A series of seven SS triaxial tests at different confining pressures (0, 5, 15, 20, 27.5, 35 and 70 MPa) were performed in which rock specimens were taken to failure under triaxial loading at a constant axial strain rate of 10^{-5}/s to measure deformational and strength properties.

Figure 4 shows the typical stress path followed in the experiments. At the beginning of each test (isotropic compression stage, IC), the confining pressure, σ_3, was increased up to the target level by multistep loading increments of 5 MPa at a constant rate of 0.33 MPa/s. After each loading increment, σ_3 was held for an hour to ensure uniform stress equilibrium (Fig. 4a). Results from the IC stage were also used to quantify geomechanical specimen variability and anisotropy (see Sects. 3.3.2 and 5.2). Once the specimen reached the equilibrium at the target confining pressure (i.e. axial and radial strains become constant), it was taken to failure (triaxial compression stage, TX) at a constant axial strain rate to measure intact strength properties. Estimation of elastic parameters is detailed in Sect. 3.3.2.

Furthermore, two additional single stage tests were conducted at different temperature levels (60 and 120 °C). These tests (SST) were performed as regular SS tests at 35 MPa of confining pressure, but involved one more phase between the isotropic and triaxial stages: the thermal consolidation stage (ThC). During this new phase, the temperature was increased to the desired value, and axial strains were allowed to stabilize before application of any differential stress q (Fig. 4b).

3.2.2 Multi Stage Triaxial Tests

Sample scarcity and variability is one of the main problems in reservoir geomechanics laboratory testing (Fjær et al. 2008; Yang 2012; Islam and Skalle 2013). Obtaining the

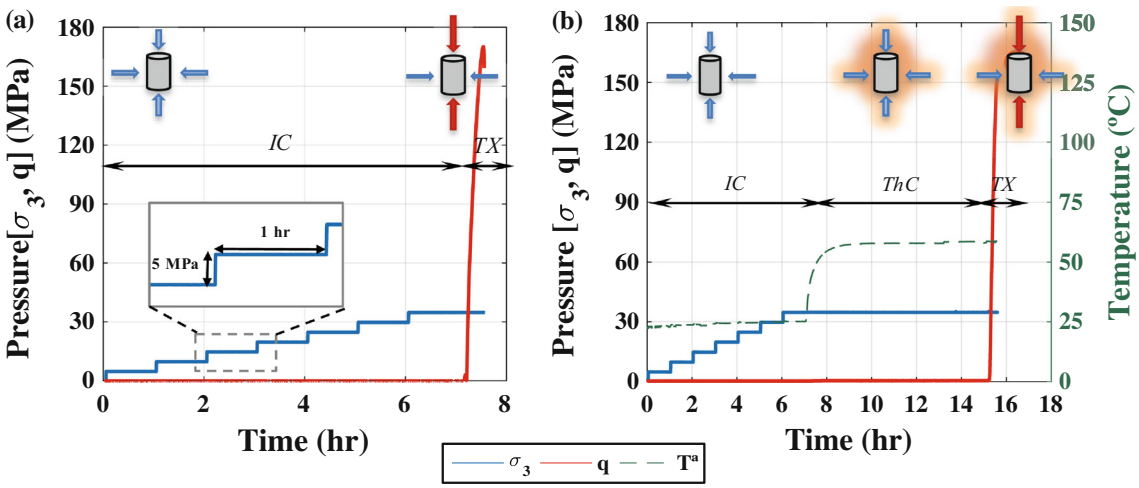

Fig. 4 Example of stress path followed during single stage triaxial tests at 35 MPa of confining pressure at **a** room and **b** high temperatures (i.e. SS35 and SST60). *IC* isotropic compression stage, *ThC* thermal consolidation stage, *TX* triaxial stage. During the IC stage σ_3 is increased by multistep loading increments of 5 MPa as shown in the detail in **a**. These loading increments are applied at a constant rate of 0.33 MPa/s

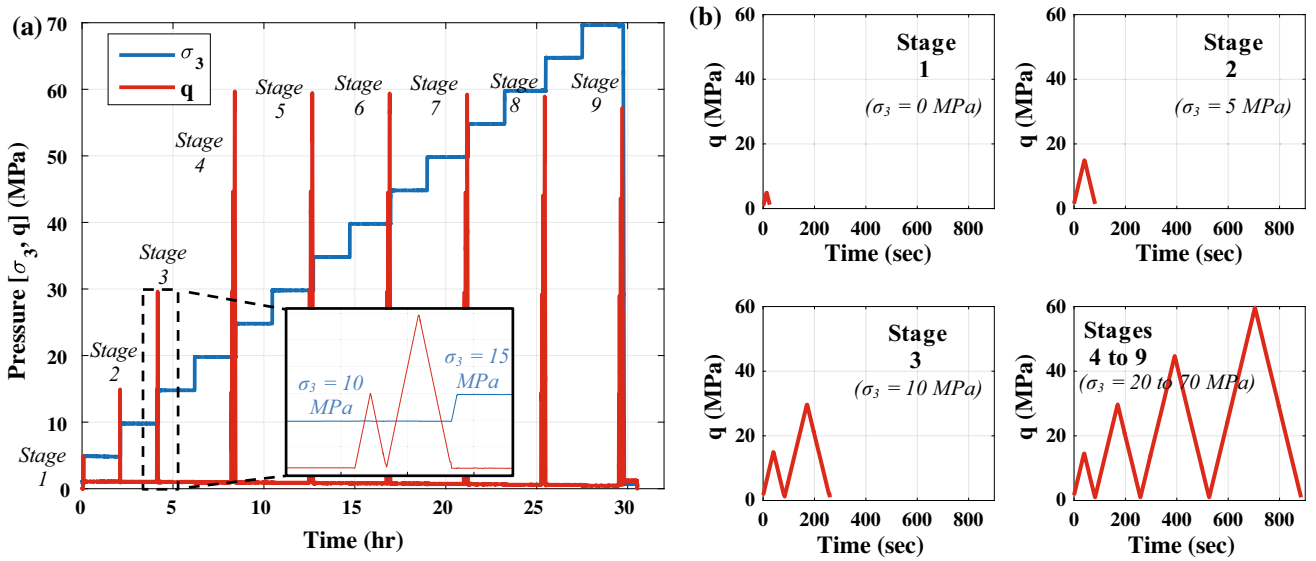

Fig. 5 **a** Elastic Multi-Stage triaxial (MSE) test consisting of nine stages at different confining pressure levels. **b** Within each stage, the differential stress was applied in 1–4 cycles increasing q from one cycle to the next one (e.g. stage 3: after the specimen reached the stress equilibrium at 10 MPa of confining pressure, q was applied in two cycles, i.e. 0 → 15 → 0 → 30 → 0 MPa, the σ_3 then increased to the next level for a new stage)

full suite of geomechanical parameters from a single core is of crucial importance. Two tests were performed in this experiment:

(a) *Elastic Multi-Stage triaxial* (MSE): Shale gas rocks are known to be non-linear materials, and the characterization of their static properties requires performing unloading–reloading cycles at different stress levels (Fjær et al. 2008). This test consisted of nine stages at different confinement levels ranging from 0 to 70 MPa (Fig. 5a). Confining pressure was increased from one stage to the next following multistep loading. Within each stage, and after the specimen was allowed to reach equilibrium at the target confining pressure, differential stress, q, was applied in one to four cycles increasing the maximum load from one cycle to the next using a loading rate of 0.33 MPa/s (stress-controlled) as shown in Fig. 5b. The differential stress, q, was always kept below 50 % UCS and three times below σ_3, so the specimen stays within the elastic range.

(b) *Failure Multi-Stage triaxial* (MSF): The goal of this test was to investigate the feasibility of predicting single-stage triaxial strength of Marcellus Shale using multi-stage triaxial data. The test was started as a single stage triaxial test (isotropic compression + triaxial loading at constant strain rate) at $\sigma_3 = 5$ MPa. When failure was detected by a significant change in the slope of the stress–strain plot, q was removed and σ_3 increased to the next level. Finally, at the last stage the specimen was taken to failure. Figure 6 illustrates the typical stress path of a failure multistage triaxial test. Loading steps were performed under strain-controlled conditions (axial strain rate of 10^{-5}/s), in contrast to the MSE in which stress-control of q was used.

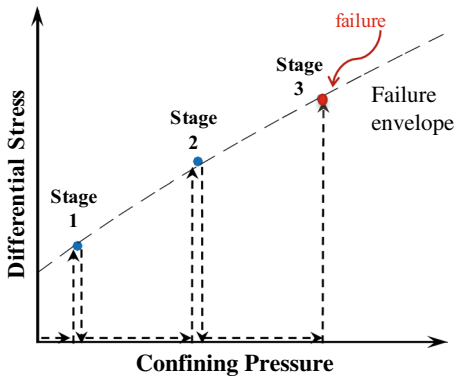

Fig. 6 Failure multi-stage triaxial (MSF) test consisted of three stages at different confinement levels; each stage was conducted as a standard (strain-controlled) triaxial test

3.3 Reversible Behavior Parameters

3.3.1 Vertical Transverse Isotropy

Shales are usually considered to be multi-scale materials composed of an anisotropic clay matrix surrounding multiple inclusions such as stiffer minerals, kerogen and microfractures (Sarout and Guéguen 2008a). The origin of anisotropy in shales has been extensively discussed in the literature (Dewhurst and Siggins 2006; Dewhurst et al.

2011; Salager et al. 2012). On the microscale, fabric anisotropy is usually defined by the preferential orientation of the clay matrix and the alignment of elongated inclusions (Sone and Zoback 2013a). At larger scales, bedding, cleavage or foliation may also affect the anisotropic behavior of these rocks. Moreover, induced anisotropy may occur after the application of anisotropic stresses, producing the development of preferential void orientations, fractures, shear planes, and faults or joints (Kuila et al. 2011; Salager et al. 2012).

Similar to many other sedimentary rocks, shales can be modeled as Vertical Transversely Isotropic (VTI) medium at the macroscopic scale. This means that the mechanical properties are equal in all directions within a horizontal plane, but different in the other directions.

Although all of the tested specimens were cored perpendicular to the bedding, and full characterization of anisotropy is not possible, in this study we still treat the shale as a VTI medium with the z-axis being the axis of symmetry (Fig. 7a). In this context, the linear elastic VTI model can be expressed in terms of five independent parameters, with the compliance matrix as follows:

$$\begin{Bmatrix} \varepsilon_{xx} \\ \varepsilon_{yy} \\ \varepsilon_{zz} \\ \varepsilon_{xy} \\ \varepsilon_{yz} \\ \varepsilon_{xz} \end{Bmatrix} = \begin{bmatrix} \frac{1}{E_h} & -\frac{\upsilon_{hh}}{E_h} & -\frac{\upsilon_{vh}}{E_v} & & & \\ -\frac{\upsilon_{hh}}{E_h} & \frac{1}{E_h} & -\frac{\upsilon_{vh}}{E_v} & & & \\ -\frac{\upsilon_{vh}}{E_v} & -\frac{\upsilon_{vh}}{E_v} & \frac{1}{E_v} & & & \\ & & & \frac{1}{G_{vh}} & & \\ & & & & \frac{1}{G_{vh}} & \\ & & & & & \frac{2(1+\upsilon_{hh})}{E_h} \end{bmatrix} \times \begin{Bmatrix} \sigma_{xx} \\ \sigma_{yy} \\ \sigma_{zz} \\ \sigma_{xy} \\ \sigma_{yz} \\ \sigma_{xz} \end{Bmatrix} \quad (1)$$

where E_h and E_v represent the Young's moduli for unconfined compression in the horizontal and vertical directions respectively; υ_{hh} and υ_{vh}, are the Poisson's ratios for strains in the horizontal direction caused by a orthogonal horizontal and vertical compressions, respectively (Fig. 7c, b); and G_{vh} stands for the shear modulus in a vertical plane (Fig. 7d).

In the context of triaxial space (for a specimen with vertical symmetry axis) x, y and z are principal axes, and only axial and radial stresses and strains are measured (i.e.

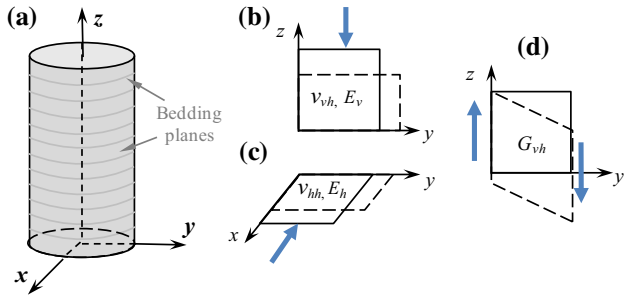

Fig. 7 Modes of shearing for vertical transversely isotropic medium. **a** VTI medium with the z axis being the axis of symmetry. Poisson's ratios for strain in the horizontal direction caused by **b** a vertical and **c** a orthogonal horizontal compression. **d** Shearing in a vertical plane

$\sigma_a = \sigma_{zz}$, $\sigma_r = \sigma_{xx} = \sigma_{yy}$, $\varepsilon_a = \varepsilon_{zz}$, and $\varepsilon_r = \varepsilon_{xx} = \varepsilon_{yy}$). Therefore, Eq. 1 for our triaxial tests is reduced to:

$$\begin{Bmatrix} \delta\varepsilon_a \\ \delta\varepsilon_r \end{Bmatrix} = \begin{bmatrix} 1/E_v & -2\upsilon_{vh}/E_v \\ -2\upsilon_{vh}/E_v & -(1-\upsilon_{hh})/E_h \end{bmatrix} \begin{Bmatrix} \delta\sigma_a \\ \delta\sigma_r \end{Bmatrix} \quad (2)$$

As a result, one can only determine E_v and υ_{vh} from triaxial tests on VTI specimens with a vertical symmetry axis (since they do appear uncoupled in Eq. 2). G_{vh} is completely missing in Eq. 2, and E_h and υ_{hh} only appear in the composite stiffness "$-(1-\upsilon_{vh})/E_h$" that relates radial strains to radial compression (Lings et al. 2000; Wood 2004). If one intends to fully determine the five independent parameters of a VTI medium from stress–strain measurements, it becomes indispensable to test specimens cored in different directions with respect bedding planes, usually vertical (0°), horizontal (90°) and oblique (45°) specimens.

Notwithstanding the above, other constitutive models have been proposed in order to study the mechanical anisotropic behavior of VTI materials with a vertical symmetry axis in the context of a triaxial test (Graham and Houlsby 1983; Puzrin 2012). For instance, Eq. 2 can be rewritten using the definitions of the triaxial strain increment and stress quantities as shown by Puzrin (2012):

$$\begin{Bmatrix} \delta\varepsilon_v \\ \delta\varepsilon_s \end{Bmatrix} = \begin{bmatrix} 1/K & -1/J \\ -1/J & 1/3G \end{bmatrix} \begin{Bmatrix} \delta p \\ \delta q \end{Bmatrix} \quad (3)$$

where, K stands for the bulk modulus during isotropic compression ($\delta q = 0$); G is the shear modulus for pure shear ($\delta p = 0$); and J is the coupling modulus. These three new parameters can be defined in terms of the original five VTI independent parameters (see "Appendix"). Furthermore, note that the non-zero off-diagonal terms show the capability of the model to reproduce both coupling between volumetric and distortional effects, and the stress path dependency of stiffness (Puzrin 2012). In this paper the use of the term stiffness refers to the material's resistance against being deformed by changes in the stress state.

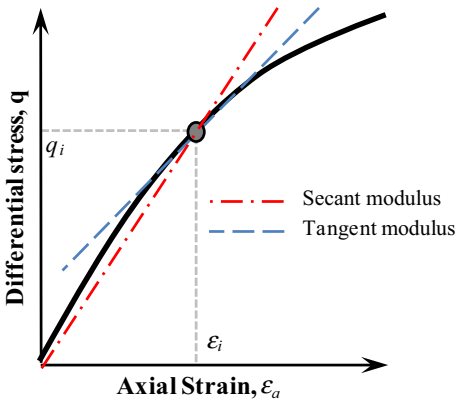

Fig. 8 Interpretation of the elastic modulus from the stress–strain relationship at a generic (ε_i, q_i) level. In this paper the tangent modulus is computed by linear regression of the data in the vicinity of the point (ε_i, q_i)

3.3.2 Estimation of Static Parameters

Defining how the interpretation of elastic moduli from the stress–strain response is accomplished becomes essential if one intends to compare moduli from different sources (Fig. 8). Commonly accepted alternatives include secant modulus, tangent modulus, or average modulus of a linear portion of the stress–strain response (Fjær et al. 2008). In this study, we used tangent modulus, which is preferred over the secant, due to its ability to describe the material response from the current stress state (Wood 2004). Among the group of elastic parameters defined above, we will address the determination of E_v, v_{vh}, K, J, and G.

From the isotropic compression stage (i.e. $\delta q = 0$), we can determine both bulk (K) and coupling moduli (J) using Eq. 3, as shown in Fig. 9a, b. Note the highly non-linear behavior, and the importance of proper interpretation of the modulus. For both K and J, the slope is estimated from the last loading stage during isotropic compression. The bulk modulus is a good index of the stiffness of the specimen prior to any differential or thermal load. Therefore K can be used to conduct a specimen variability analysis since all our specimens were subjected to the same multistep-wise loading path (up to the target σ_3) during the IC stage.

The shear modulus (G) defined in Eq. 3 can be only estimated after determining J (Fig. 9c). On the other hand, E_v and v_{vh} are determined from the triaxial stage using Eq. 2. The G, E_v and v_{vh} moduli are estimated using the tangent modulus from the linear initial portion of the stress–strain response (i.e. after closure of stress-relief microcracks).

When the rock is strongly non-linear (as it is), the mechanical behavior can hardly be represented by single-value parameters. It is often recommended to present the entire stress–strain response for complete information, and consistent interpretation of the elastic moduli may require one to perform multiple unloading–reloading cycles at different stress levels within the elastic range of the material (Fjær et al. 2008). This is not possible for the Single Stage triaxial tests (monotonic loading), but is possible for the elastic multi stage test. Figure 10 shows an example of a loading–unloading–reloading cycle. For this, the applied stress is decreased after the first-loading, and then increased again.

Lastly, it should be acknowledged that some irreversible deformation also occurs at small differential stress levels (as seen in Fig. 10) and we do therefore refer to the above-mentioned quantities as *static* moduli, avoiding the term *elastic* moduli (Fjær et al. 2008).

3.4 Irreversible Behavior Parameters

Broadly speaking, the failure process of a rock specimen subjected to uniaxial compression can be divided into several stages (Xue et al. 2014). Figure 11 shows a typical mechanical response during the triaxial stage. Typically, both axial and radial strains increase with differential stress until failure. Volumetric strain is initially dominated by

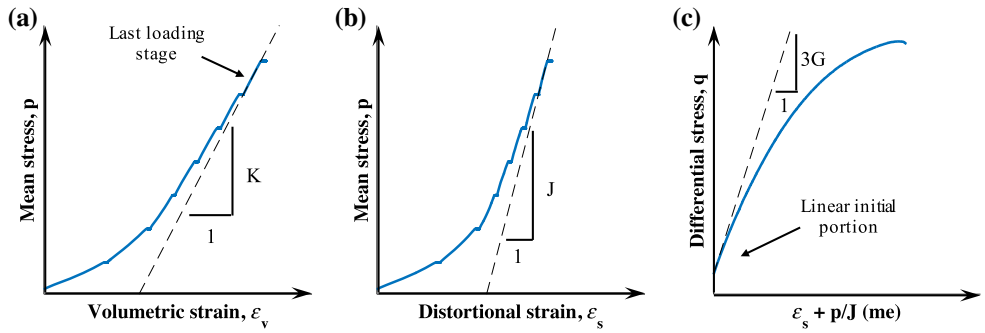

Fig. 9 Determination of VTI coupling model parameters. **a** Bulk modulus and **b** coupling modulus are estimated using the tangent modulus from the stress–strain response during the isotropic compression stage. **c** Shear modulus is estimated using the tangent modulus from initial portion the stress–strain response (i.e. after closure of stress-relief microcracks) during triaxial stage

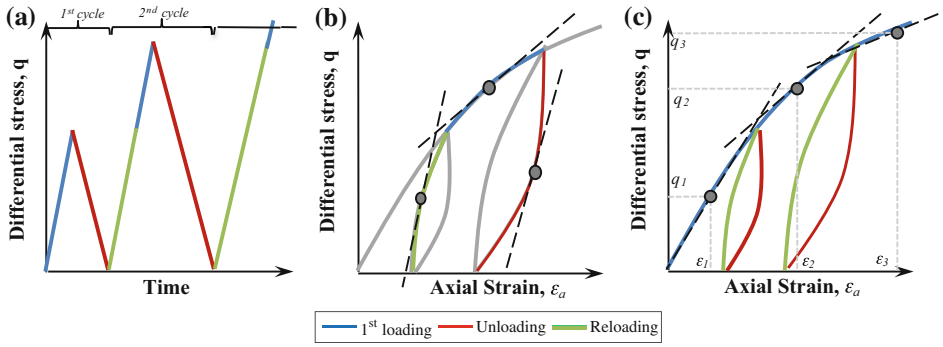

Fig. 10 Moduli determination from the elastic multi-stage triaxial test. **a** Within each stage of the MSE test, the differential stress is applied in one to four cycles. **b** Then, tangent moduli are determined from the loading, unloading and reloading portions of the stress–strain curve of each cycle. Unloading–reloading behavior show higher stiffness. Also, note that some plastic deformation occurs within the cycle. **c** Determination of the first loading Young's modulus from three different cycles. Stiffness decreases with increasing differential stress and strain levels ($E_1 > E_2 > E_3$)

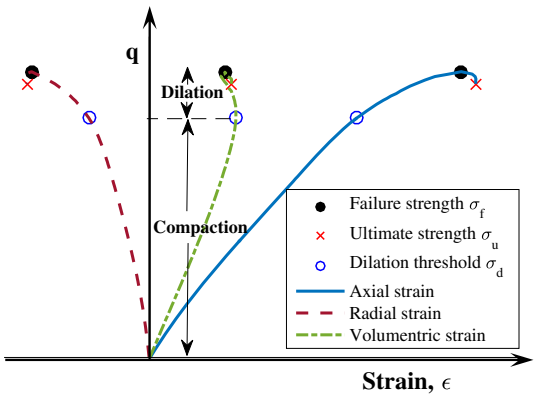

Fig. 11 Irreversible behavior parameters estimation from uniaxial compression test

compaction behavior until the dilation threshold σ_d is reached. Then, the volumetric strain is dilatancy-dominated. Depending on the material, the peak strength (σ_f) may not coincide with the ultimate strength (σ_u) which represents the stress level at macroscopic failure.

3.4.1 Failure Criteria

Two well-known and widely used criteria in rock mechanics are the Coulomb criterion (Jaeger et al. 2007) and the Empirical Hoek–Brown model (Hoek and Brown 1980). In the τ–p' space, the failure criterion can be expressed in terms of a Coulomb failure envelope by defining the coefficient of internal friction, μ_i, and the inherent shear strength (or cohesion), S_0. Since the cohesion is not a physically measurable parameter, this criterion is also written in the σ_1–σ_3 space in terms of the unconfined compressive strength (UCS or C_0) and the angle β, which gives the orientation of the failure plane with respect the maximum principal stress (i.e. the angle between the plane normal and σ_1) and is assumed to be independent of the confining pressure.

On the other hand, the non-linear Hoek and Brown criterion is able to capture the change in the slope of the failure envelope at different confining pressures. This criterion uses three model parameters: the unconfined compressive strength of the intact (i.e. unfractured) rock, C_0, and the two dimensionless parameters m and s. One drawback of this model is the lack of correlations in the literature relating m to commonly measured geophysical parameters (Zoback 2007).

4 Results

4.1 Single Stage Triaxial Tests

A summary of the test specimens for room and high temperature tests, along with the elastic and strength parameters results are presented in Table 2. Due to strain gauge loss during single stage tests at 0 and 15 MPa of confining pressure (SS00 and SS15), no radial strain data are available for these tests (axial strain was estimated from the external LVDT readings) preventing the determination of some of the elastic and strength parameters. On the other hand, the SS70 specimen was not taken to failure due to equipment limitations and, therefore, only elastic behavior was characterized at this confining pressure.

Figure 12a shows the behavior during isotropic compression of Marcellus Shale. The initial behavior is characterized by high non-linearity, reflecting the closure of pore spaces and microcracks. Due to their low permeability, fractures are likely to occur in these rocks during coring and retrieval phases, leading to macroscopic and/or microscopic fractures that may significantly impact mechanical rock behavior (Fjær et al. 2008). As confining

Table 2 Single stage triaxial test results

Test ID	Core			Test conditions		Static moduli					Strength	
	Ratio L:D	ρ (g/cc)	Depth (m)	σ_3 (MPa)	T (°C)	E_v (GPa)	ν_{vh}	K (GPa)	G (GPa)	J (GPa)	σ_d (MPa)	σ_f (MPa)
SS00	1.7	2.60	109	0	30	13	–	–	–	–	–	100.9
SS05	1.8	2.57	113	5	30	15	0.13	5	23	−9	111.9	117
SS15	1.8	2.43	112	15	30	17	–	–	–	–	–	147.9
SS20	1.8	2.56	109	20	30	18	0.13	20	9	−52	163.4	167.2
SS27.5	1.8	2.60	101	27.5	30	17	0.12	17	9	−54	179.5	186.1
SS35	1.9	2.61	100	35	30	19	0.15	19	10	−77	192.8	204.8
SS70	1.7	2.60	109	70	30	19	0.20	21	9	−90	–	–
SST60	1.7	2.61	99	35	60	19	0.15	19	9	−70	175	188.3
SST120	1.6	2.61	99	35	120	20	0.17	19	10	−69	174.2	179.8

Note that bulk modulus was estimated from the isotropic compression stage (i.e. prior to any differential/thermal load). Static moduli are estimated from the initial slope

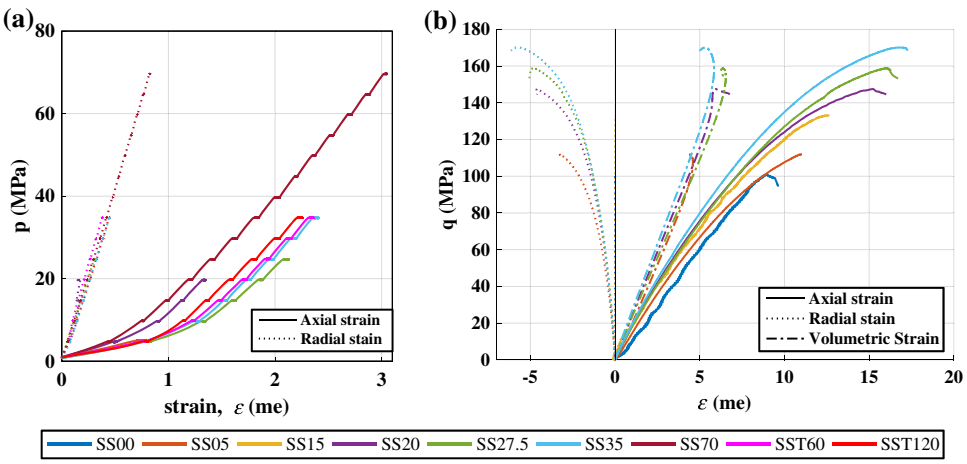

Fig. 12 Single Stage triaxial experimental results of Marcellus Shale. **a** Isotropic compression and **b** triaxial stages. Note that the *XX* in the test name (SS*XX*) corresponds to the target confining pressure (e.g. SS27.5 was conducted at $\sigma_3 = 27.5$ MPa). Also note that in tests SST60 and SST120 the isotropic compression stage was conducted under room temperature, and that σ_3 for these two test was 35 MPa. Strain units in millistrain (me)

pressure rises, an increase in stiffness is observed as expected from the further closure of microcracks. Also note the significant difference between axial and radial strains upon isotropic loading, revealing the anisotropic nature of the specimens.

Differential stress–strain plots for SS tests at room temperature can be found in Fig. 12b. For clarity, the post-ultimate portions of the data (i.e. after σ_u is reached) are not reported here. Both axial (ε_a) and radial (ε_r) strains increase monotonically with confining pressure. Also, note the initial non-linear behavior, and the small curvature of ε_a under no confinement (SS00).

Failure in these shales was found to be brittle. Except for SS27.5, sudden failure occurred accompanied by a significant drop in differential pressure. Post-mortem analyses of the cores were conducted through X-ray computed tomography (CT-scans). Figure 13 shows CT-scans images for three single stage tests at 0, 20 and 35 MPa of confining pressure. The orientation of the failure plane (β) relative to the major principal stress (coincident with cylindrical axis) was measured from these images, and found to be approximately 63°. Fracture patterns reveal that under unconfined conditions failure occurs by a combination of tensile and shear mechanisms, whereas shear is the principal failure mechanism under confinement. This suggests that confining pressure prevents the opening of vertical tensile fractures. Important to note, is the presence of planes of weakness parallel to bedding.

4.1.1 High Temperature Tests

Results of high temperature single stage triaxial tests are shown in Table 2 and Figs. 12a and 14. Prior to triaxial loading, and once the confining pressure was increased to 35 MPa following a multistep loading path (Fig. 12a), temperature was ramped to 60 and 120 °C during the

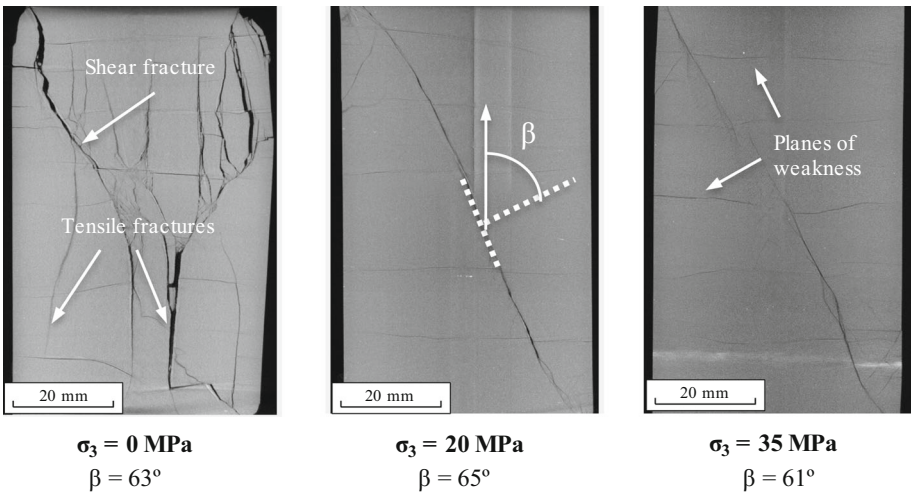

Fig. 13 Post-mortem X-ray CT-scanning images of Marcellus Shale after single stage triaxial compression experiments (room temperature). Failure under unconfined conditions occurs by a combination of tensile and shear mechanisms, whereas shear is the principal failure mechanism under confinement. Note the presence of planes of weakness parallel to bedding. β values are measured in the middle section of the core in order to avoid end-effects

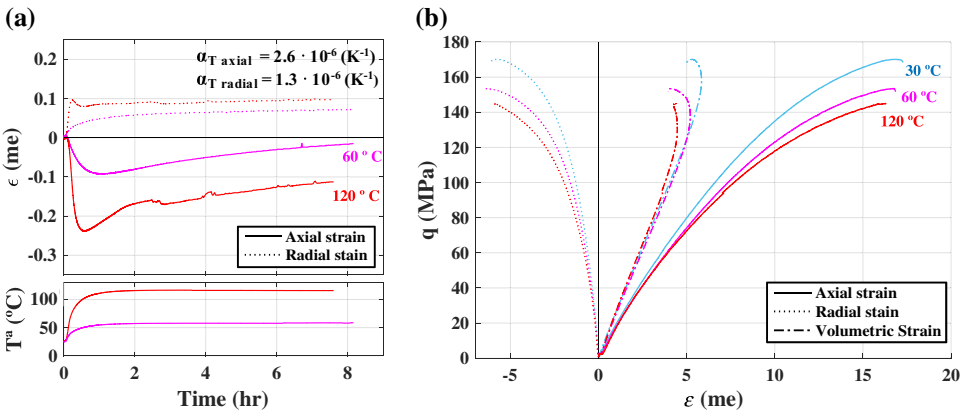

Fig. 14 High temperature tests. **a** Thermal consolidation stage. **b** Triaxial stage. Linear thermal expansion coefficients (α_T) for axial and radial directions were estimated from ThC. Strain units in millistrain (me)

thermal consolidation stage (Fig. 14a). Initially, both specimens expand axially but, even before temperature stabilizes, expansion turns into compression. On the contrary, radial strains only show compression.

Figure 14b further explores the effect of temperature on the mechanical response to differential stress. Both tests, SST60 and SST120, are compared with SS35 (room-temperature). All strength parameters (σ_d, σ_f, and σ_u) are found to decrease with increasing temperature. Fracture patterns are very similar to those identified in SS tests, and failure angles were found to be roughly 57° and 66°. We believe that any change in mechanical behavior during SST60 and SST120 tests (compared to SS35) can be directly attributed to temperature effects since both specimens showed exactly the same stiffness as SS35 during isotropic compression (Fig. 12a), and therefore specimen variability can be ruled out.

4.2 Multi-Stage Triaxial Tests

Specimen variability may indeed prevent the assessment of the impact of reservoir conditions (e.g. pressure, temperature, saturation, etc.) on the geomechanical behavior. Multi stage tests may help us to eliminate that variability. In this experiment the elastic behavior and strength properties of Marcellus Shale as a function of confining stress were studied through Elastic Multi-Stage (MSE) and Failure Multi-Stage (MSF) triaxial tests, respectively. A summary of test specimens and results is included in Table 3.

4.2.1 Elastic Multi-Stage Triaxial

Figure 15 presents the stress–strain plots for all nine stages (i.e. $\sigma_3 = 0$, 5, 10, 20, 30, 40, 50, 60, and 70 MPa) of the MSE test. A preliminary analysis reveals a significant non-linear behavior that is less pronounced as confining pressure increases. Moreover, permanent plastic deformation seems to be reduced for subsequent stages. This may be due to increasing confining pressure, successive cycling, or a combination of both. Higher confinement also decreases the non-linear behavior at higher differential stress levels (this can be easily seen in the reduction of the area enclosed between loading and unloading curves).

Table 3 Multi-stage triaxial test results. Static moduli are determined from the first$^{(L,U)}$ and second$^{(R)}$ cycles of each pressure stage (^{L,U,R}superscripts denote moduli determined from loading, unloading and reloading portions of the stress–strain curve, respectively)

Test ID	Core			Test conditions		Static moduli		Strength	
	Ratio L:D	ρ (g/cc)	Depth (m)	σ_3 (MPa)	T (°C)	E_v (GPa)	ν_{vh}	σ_d (MPa)	σ_f (MPa)
MSE	1.8	2.59	110	0	30	7^{L}–7^{U}	–	–	–
				5		11^{L}–15^{U}	0.07^{L}–0.08^{U}	–	–
				10		16^{L}–20^{U}–18^{R}	0.10^{L}–0.12^{U}–0.12^{R}	–	–
				20		20^{L}–24^{U}–22^{R}	0.14^{L}–0.15^{U}–0.14^{R}	–	–
				30		20^{L}–25^{U}–23^{R}	0.15^{L}–0.16^{U}–0.15^{R}	–	–
				40		21^{L}–25^{U}–23^{R}	0.16^{L}–0.16^{U}–0.16^{R}	–	–
				50		22^{L}–25^{U}–24^{R}	0.16^{L}–0.16^{U}–0.16^{R}	–	–
				60		23^{L}–25^{U}–25^{R}	0.16^{L}–0.16^{U}–0.16^{R}	–	–
				70		23^{L}–26^{U}–25^{R}	0.16^{L}–0.16^{U}–0.16^{R}	–	–
MSF	1.8	2.59	99	5	30	16^{L}	0.12^{L}	–	112.5
				20		20^{L}	0.14^{L}	–	161.6
				27.5		20^{L}	0.14^{L}	180.8	185.8

4.2.2 *Failure Multi-Stage Triaxial*

Results from failure multi-stage (MSF) triaxial compression test can be found in Table 3 and Fig. 16. Given the brittle nature of these shales, running this test was extremely difficult. Hence, data from only three stages ($\sigma_3 = 5$, 20 and 27.5 MPa) were recovered. Failure identification was based on visual inspection of the q–ε_a curves (Fig. 16). The post-mortem CT-scan image of MSF test (Fig. 17) shows a more fractured specimen compared to the SS test, exhibiting both shear ($\beta = 62°$) and horizontal fractures coinciding with planes of weakness.

The dilation threshold could not be obtained from the two first stages ($\sigma_3 = 5$ and 20 MPa) since differential load was removed prematurely. Nevertheless, we are confident that the specimen was very close to failure as this occurs immediately after σ_d at low confinement levels, and we believe that the differential load was removed just in the vicinity of this value.

5 Analysis and Discussion

5.1 Pressure Dependency and Non-linearity of Stiffness

Interpretation of shale stiffness (see definition in Sect. 3.3.1) from the stress–strain response of triaxial tests is not a trivial task. Firstly, the use of the term *stiffness* may be misleading because of its general association with elasticity, and with the even more general *linear elasticity* (Wood 2004), which is clearly not what we observed. Zoback and Byerlee (1975) pointed out that not only mineral elastic deformation occurs during static experiments, but also energy-dissipative inelastic deformation is induced as a result of frictional sliding and microcrack growth (Sone 2012). This additional plastic deformation clearly changes the structure of the rock, reducing the Young's modulus and reflecting material degradation. Moreover, the presence of microcracks, and other defects, may account for this non-linear behavior as well.

5.1.1 *Pressure Dependency of Stiffness*

Previous laboratory experiments and theoretical models have suggested that rock stiffness is a function of the stress state. For instance, Sarout and Guéguen (2008a) and Kuila et al. (2011) found that all ultrasonic velocities in shale increase with increasing isotropic stress. It is commonly accepted that the occurrence of cracks in rocks reduces the effective stiffness, since stress cannot be transferred across the crack itself (Fjær et al. 2008). As pressure increases, more and more cracks close resulting in a stiffer specimen.

Figures 18 and 19 show the effect of confining pressure on static moduli of Marcellus Shale (for both the coupling and VTI models, see Sect. 3.3.1).

From the isotropic stage, both bulk and coupling moduli were determined. The bulk modulus (Fig. 18a) is a good index of the stiffness of the specimen prior to any differential or thermal load, and shows consistent behavior among the tested specimens indicating low specimen variability. Initial non-linearity occurs at low confining

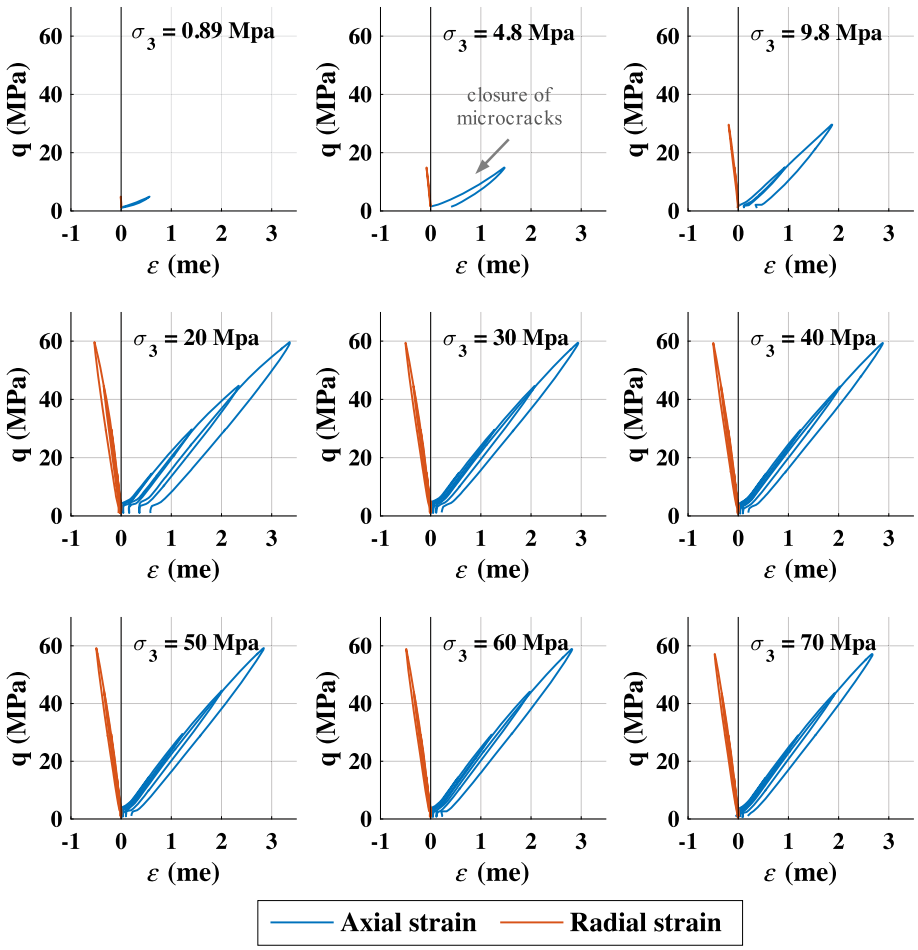

Fig. 15 Elastic multi-stage triaxial test results. Stress–strain plots for all nine stages (σ_3 = 0–70 MPa). Both permanent plastic deformation and non-linearity are reduced as confining pressure increases. Strain units in millistrain (me)

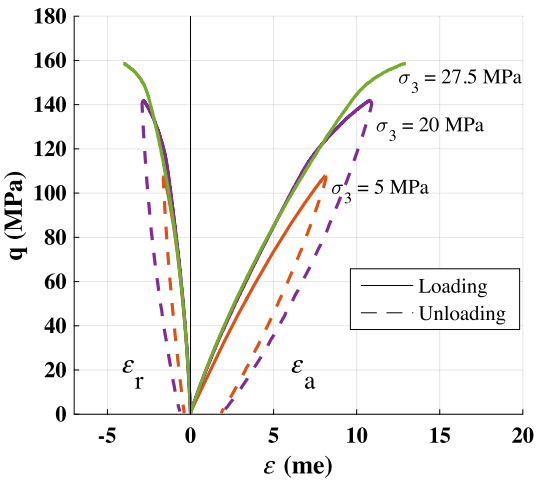

Fig. 16 Failure multi-stage triaxial test results. Differential stress vs. axial and radial strain curves for three different confinement levels (σ_3 = 5, 20 and 27.5 MPa). The sample was taken to failure at last stage. Strain units in millistrain (me)

MSF

β = 62°

Fig. 17 Post-mortem X-ray CT-scanning images of Marcellus Shale after failure multi-stage triaxial test

pressures (~15 MPa), i.e. at significantly higher-pressure levels than in situ stress (~3 MPa) at present depth (it may have been higher in the past history). However, linear increase of K is observed at higher confinement levels (20–70 MPa). Moreover, the coupling modulus (Fig. 18b) also increases with confining pressure, but following a

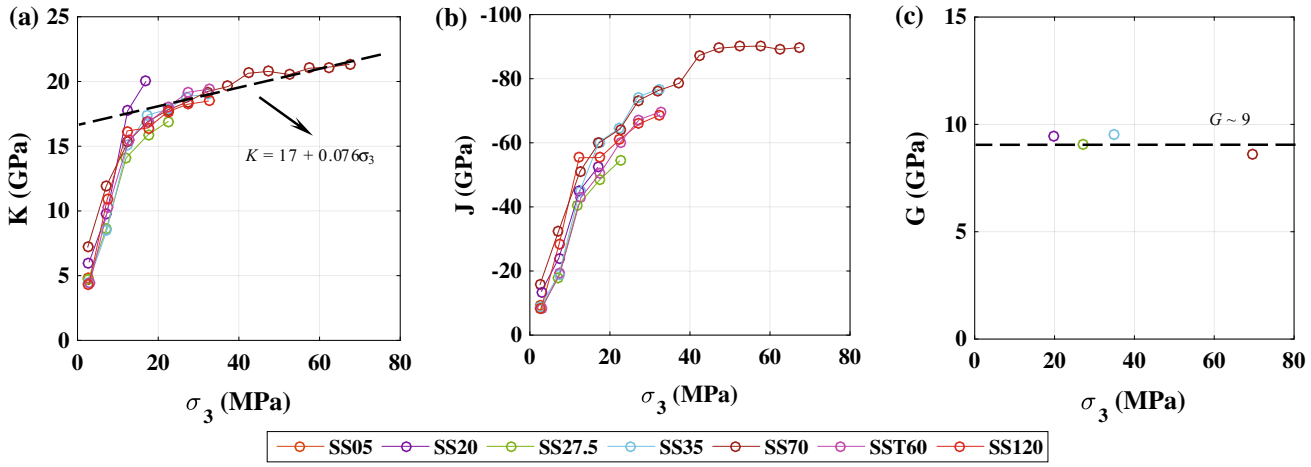

Fig. 18 Effect of confining pressure on static moduli of Marcellus Shale (coupling model parameters): **a** bulk, **b** coupling, and **c** shear moduli. Initial moduli are estimated by linear regression from Single Stage (SS) triaxial tests. Shear modulus at $\sigma_3 = 5$ MPa is not shown (see Sect. 5.2 for explanation). Also, note that K and J for the SST test are determined under room temperature conditions

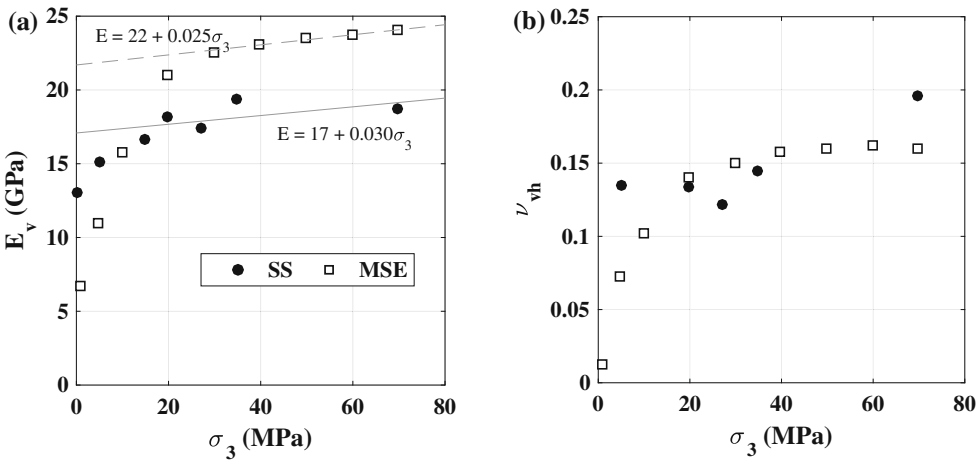

Fig. 19 Effect of confining pressure on static moduli of Marcellus Shale (VTI model). **a** Young's modulus and **b** Poisson's ratio vs. confining pressure. Initial moduli are estimated by linear regression from Single Stage (SS) and Elastic Multi-Stage (MSE) triaxial tests

different trend (it reaches a plateau around $\sigma_3 \sim 40$ MPa). On the other hand, the shear modulus (Fig. 18c) does not show any pressure dependence.

Similarly, monotonic increase is observed for Young's modulus E_v with increasing confining pressure (Fig. 19a), with important nonlinear behavior about 15 MPa of confining pressure, especially for MSE test results. This is in good agreement with the trend observed for the bulk modulus (Fig. 18a). Note that at high confinement levels, the initial moduli determined from both SS and MSE tests show a similar dependency on σ_3. Poisson's ratio ν_{vh}, on the other hand, does not show significant dependence on confining pressure (Fig. 19b), exhibiting a mean value of $\nu_{vh} \sim 0.15$. Low ν_{vh} values observed at initial stages of MSE test are likely due to the initial closure of horizontal cracks. At these stages, radial strain is almost negligible compared to axial strain.

The observed trend is consistent with previous studies: higher isotropic stress results in a monotonically stiffer rock. The differential stress, however, may have different effect, depending on the magnitude of the load and the direction relative to the bedding. Figure 20 explores the joint effect of both confining and differential pressure on the first-loading Young's modulus of Marcellus Shale, E_L. As expected, differential loading in the direction perpendicular to the bedding initially contributes to the closure of the horizontal cracks (increasing stiffness in that particular direction). This is especially evident at early stages ($\sigma_3 = 0$–10 MPa) as shown in Figs. 15 and 20. However, as the differential load increases, a reduction in the tangent Young's modulus is observed. Dependency of E_v on σ_3 at high confinement levels has an excellent agreement with empirical relationships developed in Fig. 19a.

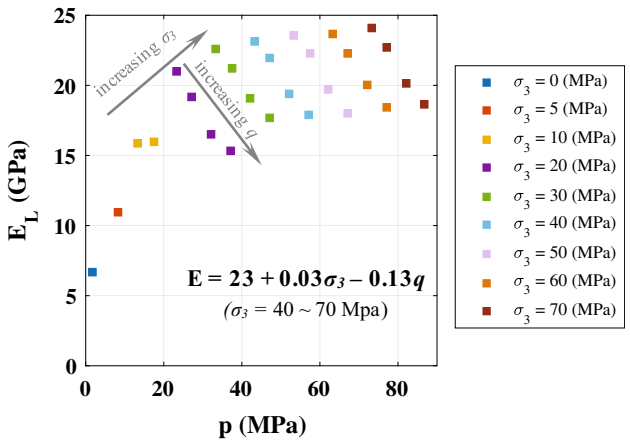

Fig. 20 Variation of tangent Young's modulus of Marcellus Shale during the Elastic Multi Stage test. Each series represents the static Young's modulus estimated during first-loading at different differential stress levels. While stiffness increases with confining pressure, σ_3, it also decreases within each stage upon differential loading. The empirical relationship $E(\sigma_3, q)$ was determined by least-squares regression from the last four stages

They initial non nonlinear behavior of K and E_v shown in Figs. 18a, 19a and 20 is likely due to the closure of cracks (Fig. 2b, g, h), Two different trends at $\sigma_3 \sim$ 0–15 MPa and $\sigma_3 \sim$ 25–70 MPa were found for K and E_v suggesting that the closure of microcracks becomes less important at high confinement levels (i.e. the increase of stiffness with confining pressure is more pronounced at lower σ_3 stages). This could be explained by the number of microcracks that remain open at different confinement levels. For instance, under low confining pressure most of the cracks are still open, while only a few microcracks remain open at high confinement levels, and hence the lower potential increase in stiffness. An alternative interpretation may be related to the potential presence of two microcracks systems with different stiffness: (1) the stress-relief and coring induced cracks (possibly visible at Fig. 2b, g scales), and (2) inherent microcracks (Fig. 2h) and pore volume systems residing within the clay and organics in the shale rock (Sone and Zoback 2013b). In such a case, the initial behavior at $\sigma_3 \sim$ 0–15 MPa found in Figs. 18a, 19a and 20 might not accurately describe the real in situ behavior.

5.1.2 Loading, Unloading and Reloading moduli

As stated in Sect. 3.3.2, the determination of the static moduli for non-linear materials can be done using multiple unloading–reloading cycles at different stress levels. In the MSE tests, first-loading and unloading parameters were estimated by linear regression from the first cycle of each stage (i.e. $q \in$ 5–15 MPa, the non-linear initial portions of the curves of Fig. 15 were neglected), while reloading parameters correspond to initial moduli of the second cycle.

Even though when they are determined over the same differential pressure magnitude (i.e. $\Delta q = 10$ MPa), Young's moduli values upon unloading (E_u) are about 12 % higher than upon loading (E_L) as shown in Table 3. This difference decreases exponentially from 33 % (at $\sigma_3 = 5$ MPa) to 8 % (at $\sigma_3 = 30$ MPa) and then stays constant, suggesting that most of plastic deformation (and/or non-linear crack closure) occurs within the four first stages of the MSE test (i.e. $\sigma_3 =$ 0–20 MPa).

It is known that loading introduces both elastic and plastic strains, which are not recovered upon unloading where mostly elastic deformation occurs. Hence, loading–reloading moduli are higher than loading ones, quite similar to dynamic estimates, and better reflect the actual elastic behavior of the rock (Zoback 2007; Sone and Zoback 2013a).

5.1.3 Non-Linear Behavior

Therefore, stiffness cannot be uniquely defined for non-linear materials, not even at a given stress level. Non-linear behavior is commonly described by stiffness vs. strain plots (Fig. 21), which are recommended to fully characterize the mechanical behavior. These plots are generated through the evaluation of the tangent modulus (Fig. 8) along the entire stress–strain (q vs. ε_a)- and radial–axial strain (ε_r vs. ε_a)-curves, for E_v and v_{vh} respectively.

Figure 21a shows a fairly linear decay of static Young's modulus with axial strain, for most part of the loading. This constant decay does not exhibit any dependence on confinement. Also, note the initial non-linear behavior (material stiffening) in SS00, SS05 and SS20 tests due the stress-relief cracks closure.

This decrease in the Young's modulus with increasing differential stress (Figs. 20, 21) is often attributed to induced plastic strains during loading, being therefore the plasticity the dominant source of nonlinearity. However, while one could attribute the apparent *stiffness softening* to the plastic strains at early stages of the MSE test (say $\sigma_3 =$ 0–20 MPa), this would not be completely true at later stages where plastic deformation is not significant (see Fig. 15). Nevertheless, a consistent decrease of E_L with differential load is observed for all stages. We should therefore acknowledge that some of the elastic properties of the shale vary with stress and strain levels (Sarout and Guéguen 2008b; Kuila et al. 2011; Dewhurst et al. 2011).

Meanwhile, Poisson's ratio (Fig. 21b) exhibits non-linear increase with axial strain up to $v_{vh} = 0.5$, a point where the dilation threshold is reached. Then, v_{vh} continues to

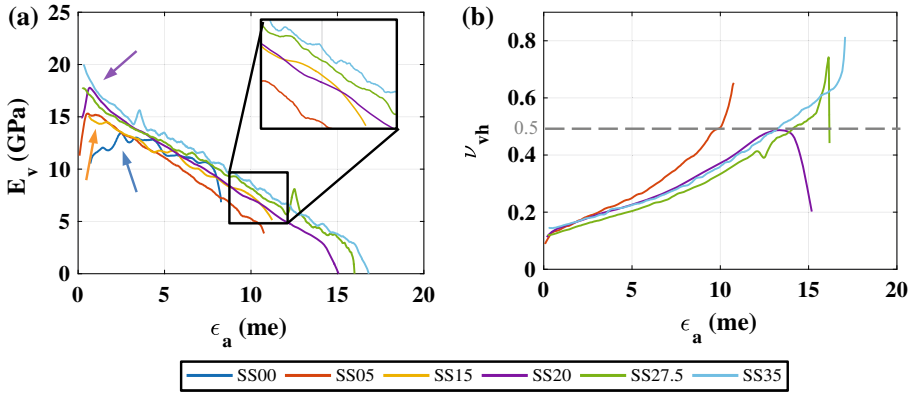

Fig. 21 Variation of tangent stiffness of Marcellus Shale in monotonic shearing during single stage tests. **a** Static Young's modulus and **b** Poisson's ratio. *Arrows* point at initial non-linear behavior (sample stiffening). These plots are generated through the evaluation of the tangent modulus (Fig. 8) along the entire stress–strain (q vs. ε_a)- and radial–axial strain (ε_r vs. ε_a)-curves, for E_v and ν_{vh} respectively. Strain units in millistrain (me)

increase at a constant rate until the failure onset, where a drastic growth occurs. This is observed for all tests but SS20, where ν_{vh} decreases after σ_d is reached. No dependency with confining pressure is observed.

Increase in Poisson's ratio reflects a growing significance of radial strains relative to axial strains ($\nu_{vh} = -\varepsilon_r/\varepsilon_a$). This could be due to a decreasing growth rate of ε_a with confining pressure (e.g. decreasing closure of horizontal microcracks, see comment in Sect. 5.1.1); increasing growth rate of ε_r (e.g. opening of new vertical cracks); or a combination of both.

5.2 Anisotropy

In this paper the mechanical behavior of Marcellus Shale rocks was studied under the assumption of VTI media. Nevertheless, there is the possibility that these specimens are also anisotropic in the horizontal plane as the entire Marcellus section was subjected to layer-parallel shortening during the Alleghanian orogeny. Previous studies have demonstrated mineral (Oertel et al. 1989) and magnetic anisotropy (Hirt et al. 1995). But since P-wave velocity anisotropy is usually less than 4 % in the horizontal plane of these shales (Evans et al. 1989), and our specimens did not show any preferential microstructure in the horizontal plane (Fig. 2c, d), VTI geometry was assumed in this analysis.

Full characterization of geomechanical behavior of VTI materials through static measurements is only possible when rock specimens cored in different directions (or true triaxial apparatus) are available. In order to get around the obstacle, we have made use of the VTI coupling model in the triaxial space (Eq. 3). This model incorporates the coupling modulus J, to acknowledge the contributions of mean and distortional stress increments to distortional and volumetric strains respectively. During isotropic compression ($\delta q = 0$), J gives us an idea of how much axial and radial strains increments differ. Recall, that for isotropic materials axial and radial strain increments are equal upon isotropic loading. Therefore, the more isotropic the material is, the higher the absolute value of J should be. Figure 18b shows the evolution of J parameter with increasing confining pressure for SS tests. However, this also accounts for the rock stiffening process. In order to address the evolution of the anisotropy, we suggest considering the index $\varepsilon_a/\varepsilon_r$ (Fig. 22). This might be a useful proxy for characterization of anisotropy when the estimation of other indices, such as Thomsen parameters (Thomsen 1986), is not possible.

As confinement increases, microfractures sub-parallel to bedding are closed first, reducing the compliance in the direction perpendicular to bedding. This gradual stiffening process in the axial direction clearly reduces the degree of anisotropy in VTI media. This is in good agreement with previous experimental studies of shale anisotropy using the single core plug method (Sarout and Guéguen 2008a; Kuila et al. 2011).

Besides providing some insights about the anisotropy evolution, the J parameter can be used along with K and G, defined in Eq. 3, in order to estimate the value of the five independent parameters which describe VTI media (i.e. E_h, E_v, G_{vh}, ν_{hh} and ν_{vh}). For instance, if we force certain interdependencies among these five parameters [i.e. $\nu_{vh} = \nu_{hh}/\alpha$; $E_h/E_v = \alpha^2$; $2G_{vh} = \alpha E_v\,(1 + \nu_{hh})$] (Graham and Houlsby 1983), Eqs. 7–9 in "Appendix" can be used to fully characterize VTI media elastic behavior. Table 4

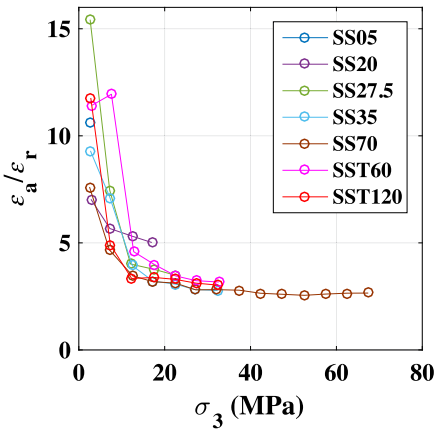

Fig. 22 Evolution of anisotropy degree with confining pressure. Note how the anisotropy degree is reduced as horizontal microcracks are closed due to increasing confinement

Table 4 VTI model parameters estimated from the coupling model (*K*–*J*–*G*)

Test ID	E_v (GPa)	E_h (GPa)	α^2	G_{vh} (GPa)	ν_{hh}	ν_{vh}
SS05	10	–	1500	–	−12.29	–
SS20	19	46	2.5	12	0.26	0.17
SS27	18	40	2.2	11	0.23	0.16
SS35	20	36	1.8	13	0.26	0.19
SS70	19	31	1.6	13	0.30	0.24

presents the values for the five VTI parameters estimated using the coupling model. Except for the SS05 test, the coupling model provides good estimates of the five VTI parameters. At low confining pressure levels (i.e. $\sigma_3 = 5$ MPa), most of horizontal microfractures remain opened, and they can be easily close upon further axial loading during triaxial stage. This results in quite different degrees of anisotropy during isotropic and triaxial stages at low confinement levels, preventing the use of the coupling model.

The anisotropy ratio, α^2, decreases from 2.5 to 1.6 as confining pressure increases from 20 to 70 MPa. This is in good agreement with previous laboratory studies on gas shales (e.g. Sone and Zoback 2013a; Ghassemi and Suarez-Rivera 2012). Whereas the error in the estimation of E_v is about 3 %, ν_{vh} estimates differ 27 % in average compared to original values shown in Table 2.

5.3 Interpretation of Failure Parameters

There are many different ways in which failure data from triaxial tests can be analyzed. For instance, Fig. 23a presents the failure data in the τ–p' space using Mohr's circles at failure for SS tests. This allows us to directly interpret both cohesion and the internal friction angle (μ_i) of the rock from the Coulomb envelope. The Coulomb failure criterion is not only one of the simplest, but also the most widely used criterion for geomaterials.

Another common way of presenting strength data is through the σ_1–σ_3 space (Fig. 23b). The unconfined compressive strength (C_0) for these rocks is about 100 MPa, and the coefficient of internal friction is close to 0.6. Moreover, the orientation of the failure surface using the Coulomb envelope, $\beta = 60.2°$, is within the observed range from the CT-scans (Figs. 13, 17). C_0 is in good agreement with the trend found by Sone and Zoback (2013a) given the clay/kerogen content and Young's modulus of our specimens.

Furthermore, we also investigated the influence of σ_3 on peak strength of Marcellus Shale using the non-linear Hoek and Brown criterion. Comparison between both Coulomb

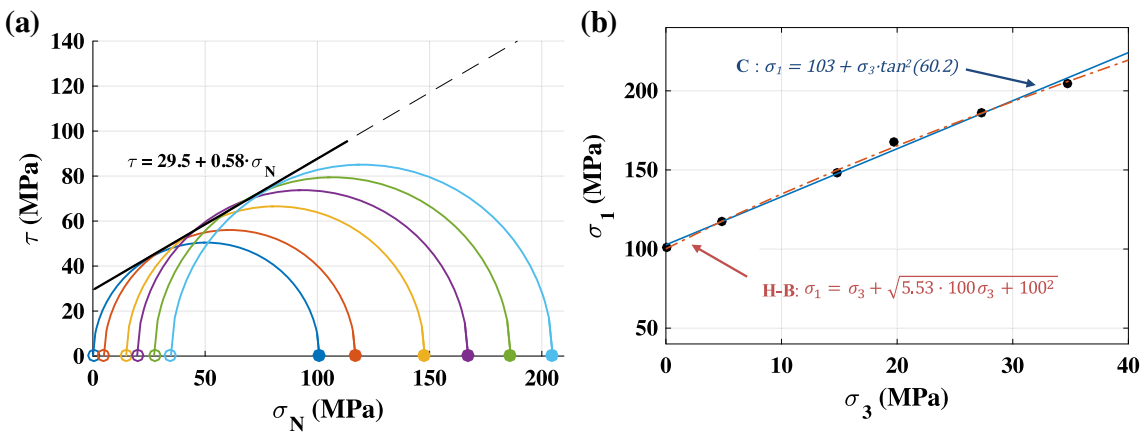

Fig. 23 Interpretation of failure parameters of Marcellus Shale (SS tests). **a** Mohr's circles and Coulomb failure envelope. **b** Comparison between the Coulomb and the empirical Hoek–Brown criteria

Table 5 Coulomb and Hoek–Brown criteria parameters for Marcellus Shale estimated by linear regression

Linearized Mohr–Coulomb criterion					Empirical Hoek–Brown criterion			
C_0 (MPa)	β (°)	S_0 (MPa)	μ_i	RMS (MPa)	C_0 (MPa)	m	s^a	RMS (MPa)
103	60.2	29.5	0.58	2.51	100	5.53	1.0	1.51

[a] Assumed

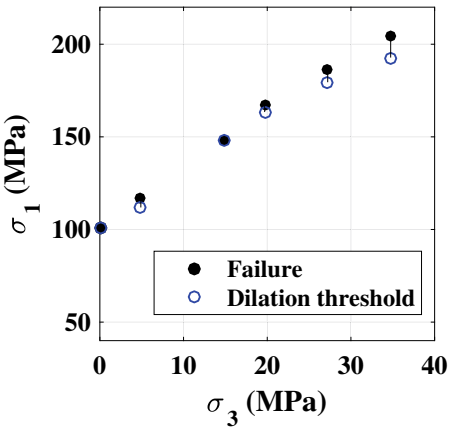

Fig. 24 Effect of confining pressure on Dilation threshold and Failure strength. *Vertical solid lines* illustrate how the difference ($\sigma_f - \sigma_d$) grows with increasing confinement

and Hoek–Brown criteria can be found in Fig. 23b. Model parameters criteria were estimated by least-square regression, and they are presented in Table 5. Within the investigated confining pressure range, both criteria are in very good agreement, with the H-B model yielding a slightly lower RMSErr.

Figure 24 presents the effect of confining pressure on both dilation threshold (σ_d) and failure strength (σ_f). While intact strength of the rock increases quite linearly with confinement, the non-linear trend of σ_d amplifies the stress difference between the onset of rock volume dilation and the failure point (i.e. $\sigma_f - \sigma_d$). This suggests that, under relatively low confinement conditions, failure occurs as soon as new fractures are opened (resulting from application of differential load), whereas increasing confining pressure prevent the rapid coalesce of newly-created microfractures and, therefore, delay failure.

5.3.1 *Multi-Stage Tests*

Failure Multi-Stage test results show that elastic moduli (Table 3) are in close agreement with those estimated from SS and MSE tests. Strength parameters followed similar trends to those obtained from SS tests (Fig. 25b), and peak strength values fall within expected range (Fig. 25a). We believe that the close agreement in both static and strength parameters is due to the relative low number of stages (3), and to the fact that the dilation threshold was not reached during the two first states. However, the more fractured core resulting from this test (Fig. 17) might suggest that additional damage occurred during the cyclic loading at high stress levels. Figure 25b shows that both axial and radial peaks have a good linear relation with the confining pressure.

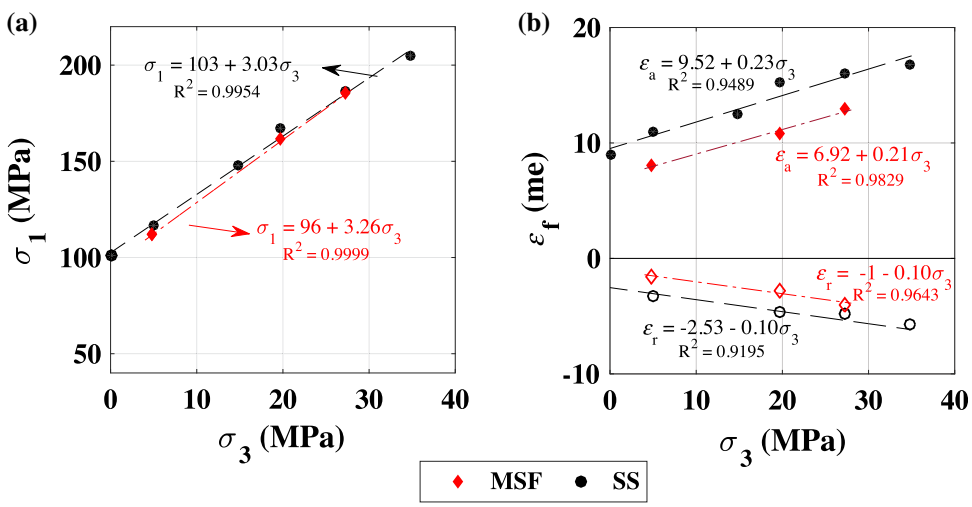

Fig. 25 Comparison of strength parameters measured during single stage (SS) and failure multi-stage (MSF) triaxial experiments. **a** Failure strength and **b** strain at failure vs. confining pressure. Strain units in millistrain (me)

5.4 Thermal Effects

The Marcellus Shale specimens tested in this study have shown a relatively small response to temperature. From the thermal consolidation (Th.C) stage, the linear thermal expansion coefficients (α_T) were estimated for both tests (Fig. 11a) revealing some anisotropic thermal expansion behavior. It is known that mica minerals and quartz (major constituents of our specimens) have a large effect on the anisotropic expansion of rocks (Huotari and Kukkonen 2004).

Experimental results show minimal change in shale static parameters and, limited strength reduction of 8 and 12 % at 60 and 120 °C respectively. Much higher strength- (approx. ~40 %) and static moduli reductions have been reported for Colorado shale tested at similar temperature conditions (Mohamadi et al. 2013). Moreover, Bauer et al. (2014) also observed much higher (up to more than 1 %) thermally-induced compression in Pierre shale. We believe that the low geomechanical response to temperature might be due to the negligible saturation of our specimens and the low kerogen content (Eseme et al. 2007).

6 Conclusions

Marcellus Shale specimens used in this study were characterized by high clay content, and moderate total organic content. Mechanical properties and porosity estimates were in good agreement with trends found for other gas shales. The fabric in these rocks exhibits primary foliation (bedding), and the microstructure reveals a clayey matrix with silt size grains and other various-shaped inclusions. The preferential orientation is preserved across scales, presenting a number of microcracks oriented sub-parallel to the bedding. It was suggested that the presence of such microcracks may affect the mechanical behavior of these shales, especially at low confinement levels.

Interpretation of stiffness in these shales is not straightforward given their significant non-linear behavior and the occurrence of small irrecoverable deformation at small stress levels. Upon isotropic loading, increase in stiffness was observed as a result of the compression process (pore volume reduction) and the closure of microcracks. Initial behavior was characterized by high non-linearity. Static moduli upon unloading were found to be systematically higher than upon loading (+12 % on average). During the triaxial stage, application of differential stress perpendicular to the bedding resulted in a linear decay of E_v with axial strain for most part of the loading. This decay did not exhibit any dependence on confinement. Nevertheless, it was observed that the elastic properties of these rocks vary with stress and strain levels. On the other hand, confining pressure seems to have a limited effect on Poisson's ratio, although this exhibited non-linear increase with monotonic axial loading. Multi stage tests were found to be useful tools for the evaluation of the mechanical behavior in non-linear materials.

The laboratory results highlighted the anisotropic nature of these shales. It has been proven that increasing confining pressure clearly reduces the degree of anisotropy. Although the specific coupling model only holds in a triaxial space with vertical symmetry axis, useful insights about specimen variability and anisotropy can be inferred from it.

As for the intact strength of these rocks, we have observed brittle failure under monotonic loading conditions. Fracture patterns revealed that failure occurs by a combination of tensile and shear mechanisms under unconfined conditions, whereas shear is the principal failure mechanism under confinement. Unconfined compression strength of the tested specimens was found to be about 100 MPa, and it falls in the low range for gas shale rocks. In contrast, the coefficient of internal friction ($\mu_i = 0.6$) was estimated to fall within the medium-upper range for shale gas rocks. Whereas the peak strength increases linearly with confining pressure, the dilation threshold shows a non-linear trend with confinement in these rocks. Both Coulomb and Hoek–Brown models fit the data very well with a very small RMSErr within the tested pressure range.

Lastly, the effect of temperature on the mechanical behavior of the solid skeleton of the shale was evaluated. Experimental results revealed a small response to thermal loading, with limited strength reduction (~10 %) and no variation of initial static moduli. We believe that this is due to the relatively low organic content and the dry conditions of our specimens.

Acknowledgments The authors would like to thank professor Terry Engelder (Geosciences Department, Penn State University) for providing the shale specimens used in this study. We appreciate the help and assistance of professors Nicolas Perdrial and Julia Perdrial (Geology Department, University of Vermont), who helped the authors with the specimen characterization. We also thank professor Mandar Dewoolkar (Civil Engineering Department, University of Vermont) for technical review and useful insights. Finally, the authors would like to acknowledge the National Science Foundation Grant 1429252 for equipment support, as well to thanks Max Graves and Howard for their assistance with X-ray tomography.

Appendix: Vertical Transversely Isotropic Three-Parameter Coupling Model

The linear elastic VTI model for a sample with the z-axis being the axis of symmetry can be expressed in terms of five independent parameters, with the compliance matrix as follows:

$$\begin{Bmatrix} \varepsilon_{xx} \\ \varepsilon_{yy} \\ \varepsilon_{zz} \\ \varepsilon_{xy} \\ \varepsilon_{yz} \\ \varepsilon_{xz} \end{Bmatrix} = \begin{bmatrix} \frac{1}{E_h} & -\frac{\upsilon_{hh}}{E_h} & -\frac{\upsilon_{vh}}{E_v} & & & \\ -\frac{\upsilon_{hh}}{E_h} & \frac{1}{E_h} & -\frac{\upsilon_{vh}}{E_v} & & & \\ -\frac{\upsilon_{vh}}{E_v} & -\frac{\upsilon_{vh}}{E_v} & \frac{1}{E_v} & & & \\ & & & \frac{1}{G_{vh}} & & \\ & & & & \frac{1}{G_{vh}} & \\ & & & & & \frac{2(1+\upsilon_{hh})}{E_h} \end{bmatrix} \times \begin{Bmatrix} \sigma_{xx} \\ \sigma_{yy} \\ \sigma_{zz} \\ \sigma_{xy} \\ \sigma_{yz} \\ \sigma_{xz} \end{Bmatrix} \tag{4}$$

In the context of triaxial space, Eq. 4 is reduced to:

$$\begin{Bmatrix} \delta\varepsilon_a \\ \delta\varepsilon_r \end{Bmatrix} = \begin{bmatrix} 1/E_v & -2\upsilon_{vh}/E_v \\ -2\upsilon_{vh}/E_v & -(1-\upsilon_{hh})/E_h \end{bmatrix} \begin{Bmatrix} \delta\sigma_a \\ \delta\sigma_r \end{Bmatrix} \tag{5}$$

Note that this compliance matrix is not symmetric since the strain increment and the stress quantities shown in Eq. 5 are not properly work conjugate. Recall that in the context of triaxial space the correctly chosen work-conjugate quantities are p–$\delta\varepsilon_v$ and q–$\delta\varepsilon_s$ for the volumetric and the distortional deformations, respectively ($\delta W = \sigma_{ij}\delta\varepsilon_{ij} = p\delta\varepsilon_v + q\delta\varepsilon_s$). Also, one can only determine E_v and ν_{vh}, but not E_h or ν_{hh} since they only appear in the composite stiffness "$-(1-\nu_{vh})/E_h$".

Equation 5 can be rewritten using the definitions of the triaxial strain increment and stress quantities as shown by Puzrin (2012):

$$\begin{Bmatrix} \delta\varepsilon_v \\ \delta\varepsilon_s \end{Bmatrix} = \begin{bmatrix} 1/K & -1/J \\ -1/J & 1/3G \end{bmatrix} \begin{Bmatrix} \delta p \\ \delta q \end{Bmatrix} \tag{6}$$

where, K stands for the bulk modulus during isotropic compression ($\delta q = 0$); G is the shear modulus for pure shear ($\delta p = 0$); and J is the coupling modulus. These three new parameters can be defined in terms of the original five VTI independent parameters (Puzrin 2012) as shown in Eqs. 7–9.

$$\frac{1}{K} = 2\frac{1-\nu_{hh}}{E_h} + \frac{1-4\nu_{vh}}{E_v} \tag{7}$$

$$\frac{1}{J} = \frac{2}{3}\left(\frac{1-\nu_{hh}}{E_h} - \frac{1-\nu_{vh}}{E_v}\right) \tag{8}$$

$$\frac{1}{G} = \frac{2}{3}\left(\frac{1-\nu_{hh}}{E_h} + 2\frac{1+2\nu_{vh}}{E_v}\right) \tag{9}$$

The compliance matrix in Eq. 6 is symmetric (material is elastic and satisfies the law of energy conservation), and the non-zero off-diagonal terms show the ability of the model to reproduce both coupling between volumetric and distortional effects, and the stress path dependency of stiffness (Puzrin 2012). However, this model is only correct in the context of the triaxial test, and only if the symmetry axis stays vertical. If one wants to model the transverse isotropy in a boundary value problem, the five independent parameters of the VTI model have to be used instead.

References

Bauer A, Holt RM, Stenebråten J, Sønstebø EF, Marøen L (2014) Thermally Induced compaction of shales. In: 48th US rock mechanics/geomechanics symposium, Minneapolis

Bažant Zdenek P, Salviato Marco, Chau Viet T, Visnawathan Hari, Zubelewicz Aleksander (2014) Why fracking works. J Appl Mech 81(10):101010. doi:10.1115/1.4028192

Britt LK, Schoeffler J (2009) The geomechanics of a shale play: what makes a shale prospective! In.: SPE eastern regional meeting, Charleston

Buscarnera G, Cusatis G, Zubelewicz A, Bažant ZP (2014) Shale fracturing for energy recovery: current issues and review of available analytical and computational models. In: Shale energy engineering, pp 168–179. doi:10.1061/9780784413654.018

Davies RJ, Mathias SA, Moss J, Hustoft S, Newport L (2012) Hydraulic fractures: how far can they go? Marine Pet Geol 37(1):1–6. doi:10.1016/j.marpetgeo.2012.04.001

Dewhurst DN, Siggins AF (2006) Impact of fabric, microcracks and stress field on shale anisotropy. Geophys J Int 165(1):135–148. doi:10.1111/j.1365-246X.2006.02834.x

Dewhurst DN, Siggins AF, Sarout J, Raven MD, Nordgård-Bolås HM (2011) Geomechanical and ultrasonic characterization of a Norwegian Sea shale. Geophysics 76(3):WA101–WA111. doi:10.1190/1.3569599

EIA (2013) U.S. Crude Oil and Natural Gas Proved Reserves

Engelder T (2009) Marcellus 2008: report card on the breakout year for gas production in the Appalachian Basin: Fort Worth Basin. Oil and Gas Magazine, p 18–22

Engelder T, Lash GG, Uzcátegui RS (2009) Joint sets that enhance production from Middle and Upper Devonian gas shales of the Appalachian Basin. AAPG Bull 93(7):857–889. doi:10.1306/03230908032

Eseme E, Urai JL, Krooss BM, Littke R (2007) Review of mechanical properties of oil shales: implications for exploitation and basin modelling. Oil Shale 24(2):159–174

Evans KF, Oertel G, Engelder T (1989) Appalachian stress study, 2. Analysis of Devonian shale core: some implications for the nature of contemporary stress variations and Alleghanian deformation in Devonian rocks. J Geophys Res 94:7155–7170

Ferrari A, Laloui L (2013) Advances in the testing of the hydro-mechanical behaviour of shales. In: Laloui L, Ferrari A (eds) Multiphysical testing of soils and shales. Springer, Berlin, pp 57–68

Fisher K, Warpinski N, Service PAH (2012) Hydraulic-fracture-height growth: real data. SPE Production and Operations

Fjær E, Holt RM, Horsrud P, Raaen AM, Risnes R (2008) Petroleum related rock mechanics, 2nd edn. Elsevier, Amsterdam

Ghassemi A, Suarez-Rivera R (2012) Sustaining fracture area and conductivity of gas shale reservoirs for enhancing long-term production and recovery, College Station

Graham J, Houlsby GT (1983) Anisotropic elasticity of a natural clay. Geotechnique 33:165–180

Hirt AM, Evans KF, Engelder T (1995) Correlation between magnetic anisotropy and fabric for Devonian shales on the Appalachian Plateau. Tectonophysics 247(1–4):121–132. doi:10.1016/0040-1951(94)00176-a

Hoek E, Brown ET (1980) Empirical strength criterion for rock masses. J Geotech Eng Div. doi:10.1016/0148-9062(81)90766-X

Horsrud P (2001) Estimating mechanical properties of shale from empirical correlations

Hu M, Hueckel T (2013) Environmentally enhanced crack propagation in a chemically degrading isotropic shale. Géotechnique 4:313–321

Huotari T, Kukkonen I (2004) Thermal expansion properties of rocks: Literature survey and estimation of thermal expansion coefficient for olkiluoto mica gneiss. Technical report, Geological Survey of Finland

Islam MA, Skalle P (2013) An experimental investigation of shale mechanical properties through drained and undrained test mechanisms. Rock Mech Rock Eng 46(6):1391–1413. doi:10.1007/s00603-013-0377-8

Jacobi D, Gladkikh M, Lecompte B, Hursan G, Mendez F, Longo J, Ong S et al (2008) Integrated petrophysical evaluation of shale gas reservoirs. In: CIPC/SPE gas technology symposium 2008 joint conference. SPE, Calgary

Jaeger JC, Cook NGW, Zimmerman RW (2007) Fundamentals of rock mechanics, 4th edn. Blackwell Publishing, Malden

Josh M, Esteban L, Delle Piane C, Sarout J, Dewhurst DN, Clennell MB (2012) Laboratory characterisation of shale properties. J Pet Sci Eng 88:107–124. doi:10.1016/j.petrol.2012.01.023

Kargbo DM, Wilhelm RG, Campbell DJ (2010) Natural gas plays in the Marcellus Shale: challenges and potential opportunities. Environ Sci Technol 44(15):5679–5684. doi:10.1021/es903811p

King G, Haile L, Shuss J, Dobkins T (2008) Increasing fracture path complexity and controlling downward fracture growth in the Barnett shale. In: SPE shale gas production conference, Fort Worth, pp 1–8. doi:10.2118/119896-MS

Kuila U, Dewhurst DN, Siggins AF, Raven MD (2011) Stress anisotropy and velocity anisotropy in low porosity shale. Tectonophysics 503(1–2):34–44. doi:10.1016/j.tecto.2010.09.023

Lacazette A, Engelder T (1992) Fluid-driven cyclic propagation of a joint in the Ithaca siltstone, Appalachian Basin, New York. In: Evans B, Wong T-F (eds) Fault mechanics and transport properties of rocks. Academic Press, London, pp 297–324

Lings ML, Pennington DS, Nash DFT (2000) Anisotropic stiffness parameters and their measurement in a stiff natural clay. Geotechnique 50(2):165–180

Mavko G, Mukerji T, Dvorkin J (2009) The rock physics handbook. tools for seismic analysis of porous media, 2nd edn. Cambridge University Press, New York

Maxwell S (2011) Microseismic hydraulic fracture imaging: the path toward optimizing shale gas production. Lead Edge 30(3):340–346

Mohamadi M, Gong X, Wan RG (2013) Laboratory and constitutive modeling of Colorado shale at high pressure and temperature. In: American Rock Mechanics Association (ed) 47th US rock mechanics/geomechanics symposium, San Francisco, pp 1–8

Morgan SP, Einstein HH (2014) The effect of bedding plane orientation on crack propagation and coalescence in shale. In: 48th US rock mechanics/geomechanics symposium, Minneapolis

Oertel G, Engelder T, Evans K (1989) A comparison of the strain of crinoid columnals with that of their enclosing silty and Shaly matrix on the Appalachian Plateau, New-York. J Struct Geol 11(8):975–993

Passey QR, Bohacs KM, Esch WL, Klimentidis R, Sinha S, Exxonmobil Upstream (2010) From oil-prone source rock to gas-producing shale reservoir—geologic and petrophysical characterization of unconventional shale-gas reservoirs." In: CPS/spe international oil & gas conference and exhibition in China 2010. SPE, Beijing, pp 1707–1735

Puzrin AM (2012) Constitutive modelling in geomechanics. Springer, Berlin. doi:10.1007/978-3-642-27395-7

Rickman R, Mullen M, Petre E, Grieser B, Kundert D (2008) A practical use of shale petrophysics for stimulation design optimization: All shale plays are not clones of the Barnett shale. In: SPE annual technical conference and exhibition, Denver

Safari R, Huang J, Mutlu U (2014) 3D analysis and engineering design of pulsed fracturing in shale gas reservoirs. In: 48th US rock mechanics/geomechanics symposium, Minneapolis, pp 1–12

Salager S, François B, Nuth M, Laloui L (2012) Constitutive analysis of the mechanical anisotropy of opalinus clay. Acta Geotech 8(2):137–154. doi:10.1007/s11440-012-0187-2

Sarout J, Guéguen Y (2008a) Anisotropy of elastic wave velocities in deformed shales: part 1—experimental results. Geophysics 73(5):D75–D89. doi:10.1190/1.2952744

Sarout J, Guéguen Y (2008b) Anisotropy of elastic wave velocities in deformed shales: part 2—modeling results. Geophysics 73(5):D91–D103

Savalli L, Engelder T (2005) Mechanisms controlling rupture shape during subcritical growth of joints in layered rocks. Bull Geol Soc Am 117(3–4):436–449. doi:10.1130/B25368

Schmitt L, Forsans T, Santarelli FJ (1994) Shale testing and capillary phenomena. Int J Rock Mech Min Sci Geomech Abstr 31(5):411–427

Sone H (2012) Mechanical properties of shale gas reservoir rocks and its relation to the in-situ stress variation observed in shale gas reservoirs. Standford University, Standford

Sone H, Zoback MD (2013a) Mechanical properties of shale-gas reservoir rocks—part 1: static and dynamic elastic properties and anisotropy. Geophysics 78(5):D381–D392. doi:10.1190/geo2013-0050.1

Sone H, Zoback MD (2013b) Mechanical properties of shale-gas reservoir rocks—part 2: ductile creep, brittle strength, and their relation to the elastic modulus. Geophysics 78(5):D393–D402. doi:10.1190/geo2013-0051.1

Thomsen L (1986) Weak elastic anisotropy. Geophysics 51:1954–1966

Vermylen JP (2011) Geomechanical studies of the Barnett shale, Texas, USA. Standford University, Standford

Villamor Lora R (2015) Geomechanical characterization of Marcellus Shale. University of Vermont, Vermont

Wood DM (2004) Geotechnical modelling. Taylor & Francis, Abingdon. doi:10.4324/9780203477977

Xue Lei, Qin Siqing, Sun Qiang, Wang Yuanyuan, Lee Lee Min, Li Weichao (2014) A study on crack damage stress thresholds of different rock types based on uniaxial compression tests. Rock Mech Rock Eng 47(4):1183–1195. doi:10.1007/s00603-013-0479-3

Yang Sheng-qi (2012) Strength and deformation behavior of red sandstone under multi-stage triaxial compression. Can Geotech J 49(May):694–709. doi:10.1139/T2012-035

Zoback MD (2007) Reservoir geomehanics. Cambridge University Press, Cambridge

Zoback MD, Byerlee JD (1975) The effect of cyclic differential stress on dilatancy in Westerly Granite under uniaxial and triaxial conditions. J Geophys Res 80:1526–1530